Self-assembly of CIP4 drives actin-mediated asymmetric pit-closing in clathrin-mediated endocytosis

Yiming Yu[1], Takuma Ozaki[1], and Shige H. Yoshimura[1*]

[1] Graduate School of Biostudies, Kyoto University, Kyoto, Japan, 606-8501

*Corresponding author

E-mail: yoshimura@lif.kyoto-u.ac.jp

Tel & Fax: +81-75-753-7906

Summary

Clathrin-mediated endocytosis plays a pivotal role in signal transduction pathways between the extracellular environment and the intracellular space. Accumulating evidence from live-cell imaging and super-resolution microscopy of mammalian cells suggests an asymmetric distribution of actin fibers near the clathrin-coated pit, which induces asymmetric pit-closing, rather than radial constriction. However, detailed molecular mechanisms of this "asymmetricity" remain elusive. Herein, we used high-speed atomic force microscopy to demonstrate that CIP4, a multidomain protein with a classic F-BAR domain and intrinsically disordered regions, is necessary for asymmetric pit-closing. Strong self-assembly of CIP4 via intrinsically disordered regions, together with stereospecific interactions with the curved membrane and actin-regulating proteins, generates a small actin-rich environment near the pit, which deforms the membrane and closes the pit. Our results provide a mechanistic insight into how spatio-temporal actin polymerization near the plasma membrane is promoted by a collaboration of disordered and structured domains.

Key Words: Cdc42-interacting protein 4; F-BAR domain-containing protein; clathrin-mediated endocytosis; high-speed atomic force microscopy; superresolution structural illumination microscopy; phase separation; actin

41 # Introduction

42 Clathrin-mediated endocytosis (CME) is necessary for several cellular processes including the uptake of low-
43 density lipoprotein, the transduction of epidermal growth factor receptor signaling, the formation of synaptic
44 vesicles, and cell migration [1-6]. Clathrin-dependent endocytic machinery is highly disciplined in the recruitment
45 and disassembly of more than 60 endocytic proteins in an ordered sequence [7-9]. The initiation of clathrin-coated
46 pits (CCPs) requires the assembly of several adaptors and scaffold proteins including the Fes/Cip4 homology
47 Bin/amphiphysin/Rvs (F-BAR) domain-only protein, AP2 complex, intersectin, and clathrin [10-14]. Polymerized
48 clathrin forms a hexagonal lattice that curves the plasma membrane and gradually drives the invagination of
49 CCP [15,16]. In the late stage of CME, highly invaginated CCPs are detached from the membrane by dynamin-
50 mediated constriction and scission, and then transported to the cytosol for further processing [17,18].

51 The pit-closing step of CME has recently attracted much attention from researchers because of the series
52 of processes involved, including membrane deformation, fusion, and scission. In addition to a canonical
53 dynamin-dependent constriction mechanism [17,18], actin plays critical roles in both yeast and mammals [19]. In
54 yeast cells, actin assembles symmetrically at the base of the CCP in a radial distribution and constricts the
55 membrane tubule [20]. In mammalian cells, actin functions as a force generator that counteracts membrane tension,
56 elongates the membrane tubules, and assists in the formation of deeply-invaginated vesicles [21-23]. Furthermore,
57 actin coordinates other endocytic proteins such as dynamin and BAR domain proteins to promote the
58 constriction and scission of the membrane tubules before the translocation of vesicles [24-26].

59 Recent progress in various imaging techniques revealed an asymmetric distribution of actin near the
60 CCP [22,27]. Electron and super-resolution microscopy identified actin and some associated proteins, including the
61 neural Wiskott–Aldrich syndrome protein (N-WASP) and actin-related proteins-2/3 (Arp2/3) complex,
62 asymmetrically assembling near the CCP [22,27,28]. Correspondingly, live-cell imaging with ion conductance
63 microscopy revealed a membrane bulge that formed asymmetrically around the CCP and gradually covered that
64 area [29]. Correlative imaging of high-speed atomic force microscopy (HS-AFM) and confocal laser-scanning
65 microscopy (CLSM) demonstrated that the asymmetric closing process was actin-dependent [30]. Because a lateral
66 constriction is energetically more favorable for membrane fusion than a radial constriction [31], the actin-

67 dependent asymmetric closing mechanism seems to play a major role in CME; however, the detailed molecular
68 mechanism generating asymmetric assembly of actin machinery remains elusive.

69 Herein, we studied the molecular mechanism underlying asymmetric actin assembly and the consequent
70 generation of the membrane bulge near the CCP. We used live-cell HS-AFM and fluorescence-based imaging
71 techniques to examine the involvement of F-BAR domain-containing proteins (CIP4, FBP17, and Syndapin 2),
72 which carry structured domains to interact with actin regulatory proteins as well as long, disordered domains,
73 and are known to be involved in CME. Our results provide mechanistic insights into how a multi-domain protein
74 can spatio-temporally recruit and orchestrate the actin machinery near the CCP via phase separation of
75 disordered domains and stereospecific interactions between structured domains.

76

77 # Results

78 **Asymmetric closing of the CCP**

79 Using HS-AFM, CME was described as a group of near-circular invaginations with diameters ranging from 150
80 to 400 nm and lifetimes ranging from 40 to ~300 s [30]. This prior observation revealed a variety of dynamic
81 processes of the plasma membrane during the CME. Three different closing patterns: "asymmetric,"
82 "symmetric," and "undetermined," were identified (Figure 1A and Figure S1A–C). The asymmetric pattern is
83 the dominant closing pattern that corresponds to ~71 % of total closing events (Figure 1B), in which a membrane
84 bulge emanates from one side (or a limited area) of the CCP, and covers the pit at the end (Figure 1A, Figure
85 S1A, and Video S1). The diameter of the pit plummeted within 10–20 s before complete closing (Figure 1A and
86 C and Figure S1A). In the symmetric pattern (~18 % of total events, Figure 1B), the pit slowly shrank
87 isotropically and completely closed with a weak membrane bulge (Figure 1A and C and Figure S1B). There
88 was a small portion of the pits (~10 % of the total events, Figure 1B) that closed within 10–20 s but without any
89 detectable bulges (Figure 1A and C and Figure S1C). Even under the scanning with a higher time resolution
90 (0.5 frames/s), a membrane bulge was not observed around these pits (Figure S1D); therefore they were
91 classified as "undetermined."

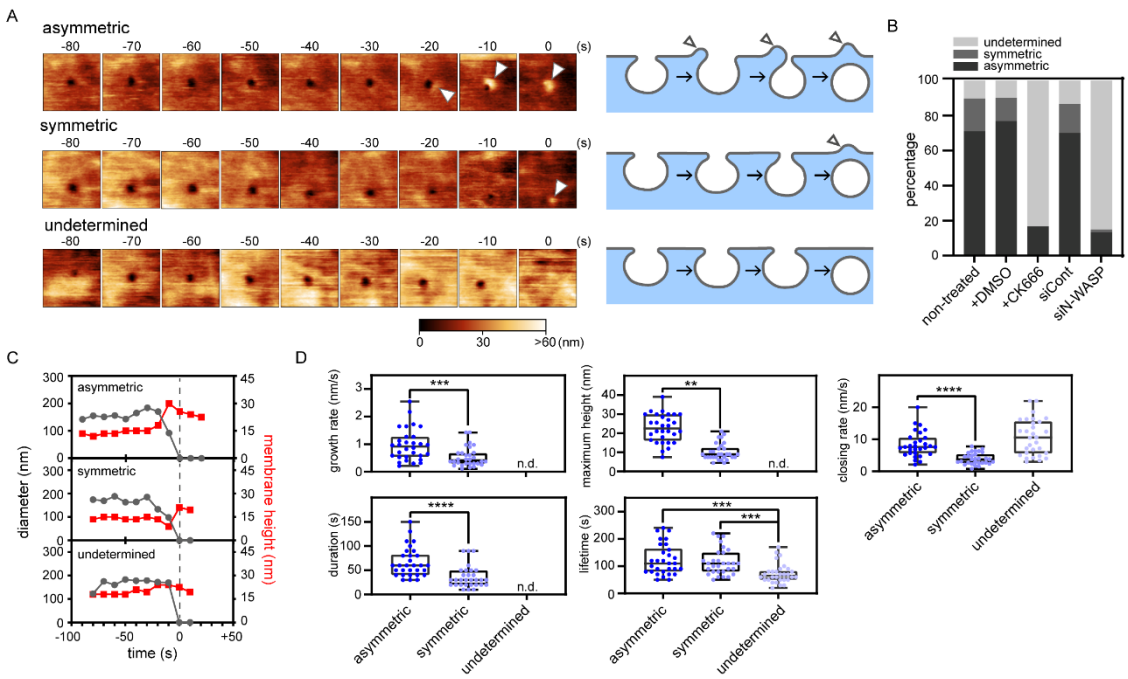

Figure 1. Asymmetric closing pattern of the CCP.

A. Time-lapse HS-AFM images and schematic illustrations of the asymmetric, symmetric, and undetermined closing patterns of CCP identified in Cos7 cells. Images were taken every 10 s. Time 0 was defined as the time point when the pit completely closed on the HS-AFM image. The membrane bulge is indicated by arrowheads and the height information of the AFM image is presented using a color bar. Image size: 1.0 × 1.0 μm^2. Representative images are presented here, and additional images are provided in Figure S1A–C.

B. The ratio of the three CCP closing patterns in non-treated Cos7 cells (N = 98), Cos7 cells treated with DMSO (N = 60) or CK666 (N = 60), and Cos7 cells transfected with siRNA for the control (luciferase) (N = 60) or N-WASP (N = 60).

C. The diameter of CCP (black) and the maximum membrane height at the pit area (red) were plotted against time in three different closing patterns. A representative case is shown in (A). Additional cases are shown in Figure S1A–C. Time 0 was defined as the time when the pit completely closed and is indicated with a black dotted line.

D. The growth rate, maximum height and duration of the bulge, and the total lifetime and the closing rate of CCP in individual closing patterns were plotted (N = 30, for each condition). The median, lower quartile, and upper quartile values are shown in the box and the minimum and maximum values are indicated with upper and lower whiskers, respectively. In undetermined cases, the height, duration, and growth rate of the membrane bulge were not defined (n.d.). Statistical analysis was performed using the Student's t-test, $\alpha = 0.05$; **:$P < 0.01$; ***: $P < 0.001$; ****: $P < 0.0001$.

Please also refer to Figure S1, and Video S1.

The asymmetric bulge grew faster (increment of the membrane height per unit time), higher (the maximum height of the bulge), and continued for a longer period (duration of the bulge) than the symmetric bulge (Figure 1D), but both patterns had a similar total lifetime (Figure 1D). The closing rate (reduction of the diameter per unit time) also differed: the asymmetric pattern (8.3 ± 3.9 nm/s) was faster than the symmetric one (3.9 ± 1.8 nm/s) (Figure 1D), suggesting that the asymmetric bulge may accelerate the pit closure compared to that of the symmetric bulge. Treatment with CK666, an inhibitor of the Arp2/3 complex [32,33], and the knockdown of N-WASP (Figure S1E), an upstream activator of Arp2/3 [34], promoted the formation of CCP while reducing the frequency of both asymmetric and symmetric bulges to < 20 % and ~0 %, respectively (Figure 1B and Figure

100 S1F and G). This demonstrates that N-WASP and Arp2/3-dependent actin polymerization are required for bulge
101 formation.
102
103 **CIP4 is necessary for the asymmetric bulge**
104 We further identified the proteins that potentially mediate the asymmetric closing process. Owing to their
105 membrane deformation and actin-associated properties, F-BAR domain-containing proteins served as ideal
106 candidates to coordinate actin reorganization with membrane deformation during CME [26,35-37]. CIP4, Syndapin
107 2 (Synd2), and FBP17 are classic F-BAR domain proteins localized at CCPs [9-14], and Cos7 cells express all
108 these proteins (Figure S2A and B). The time-lapse fluorescence observations of Cos7 cells expressing mCherry-
109 fused CIP4, Synd2, or FBP17 together with enhanced green fluorescent protein (EGFP)-fused clathrin light
110 chain B (CLTB) revealed different timings and kinetics of their assembly at the CCP (Figure 2A and Figure
111 S3A–C). When the disappearance of the clathrin signal was set as time 0, CIP4, Synd2, and FBP17 appeared at
112 the CCP at -26.0 ± 7.4, -16.0 ± 5.5, and -10.5 ± 4.0 s and disassembled at -5.0 ± 2.3, -7.8 ± 4.4, and -2.0 ± 6.0
113 s, respectively (Figure 2B). Knockdown of CIP4 in Cos7 cells (Figure S2C) reduced the frequency of the
114 asymmetric bulges (from ~74 to ~20 %) and increased the undetermined pattern (~70 %) (Figure 2C and Figure
115 S2D). In contrast, the knockdown of Synd2 or FBP17 did not greatly affect any closing patterns (Figure 2C and
116 Figure S2D). Nevertheless, the overall frequency of CME was not affected (Figure S2E). These results
117 demonstrated that CIP4, but not FBP17 or Synd2, is necessary for the asymmetric bulge.
118 Correlative imaging of HS-AFM and CLSM revealed a clear correlation between the assembly of
119 CIP4 and the bulge formation. When the complete closure of the pit under the HS-AFM was set as time 0, CIP4
120 appeared at -12.3 ± 7.25 s under CLSM, and the membrane bulge formed at -10.8 ± 6.40 s under the HS-AFM
121 (Figure 2D and Figure S2F), indicating a close correlation between CIP4 and the bulge formation.
122 To confirm the asymmetric localization of CIP4, the relative position of CIP4 and the clathrin signal
123 was determined using time-lapse super-resolution structural illumination microscopy (SIM). The CIP4 signal
124 started to appear at the determined position offset from clathrin (center-to-center distance within the first 5 s,
125 126.8 ± 66.6 nm, N = 160) (Figure 2E and F). As the CIP4 signal increased, the center-to-center distance
126 fluctuated with a decreasing tendency until both signals disappeared (Figure 2E and Figure S2G). Based on
127 these observations, we concluded that CIP4 was asymmetrically assembled at the site of CME.

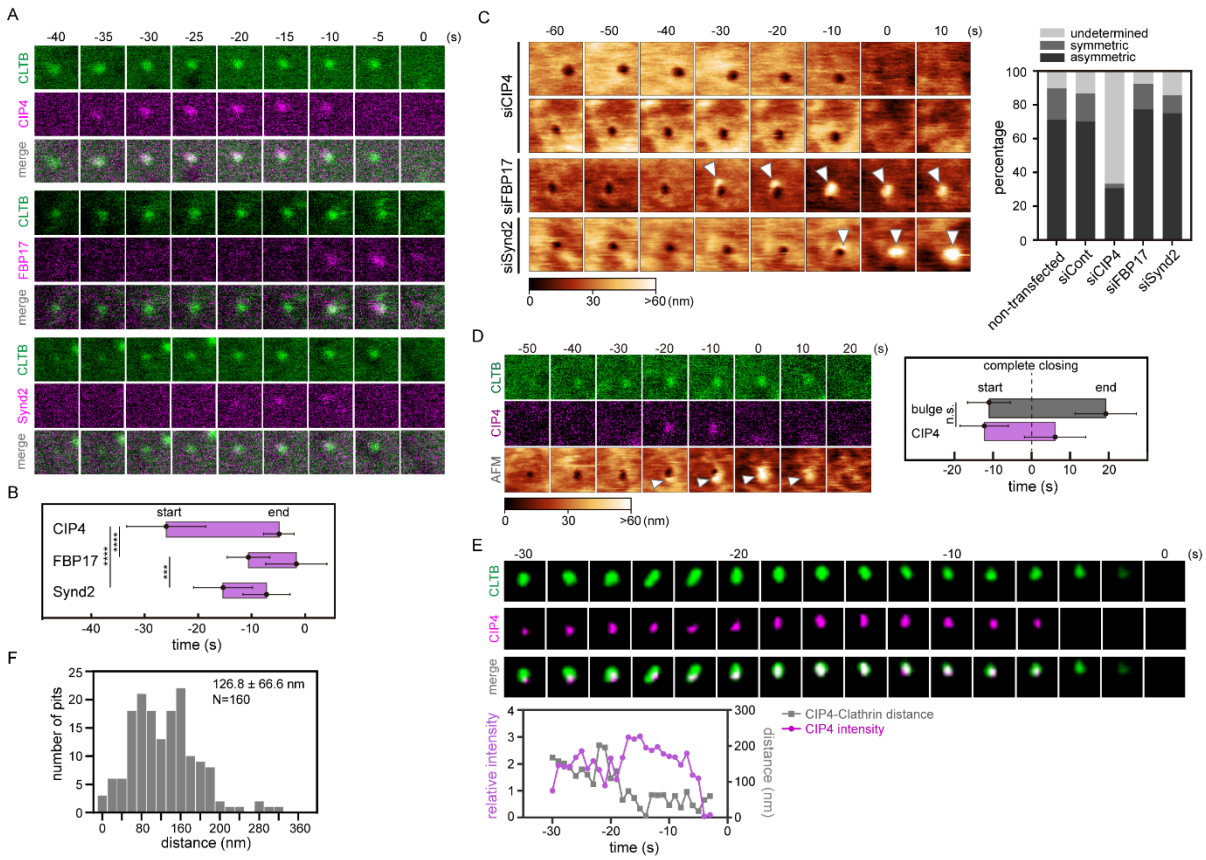

Figure 2. CIP4 is necessary for the asymmetric bulge.

A. Time-lapse fluorescence images obtained from Cos7 cells expressing EGFP-fused CLTB and mCherry-fused CIP4, FBP17, or Synd2. Images were acquired every 5 s. Image size: 1.0 × 1.0 μm^2. Time 0 was defined as the time when the clathrin signal disappeared. Representative images are presented here, and additional images are provided in Figure S3A–C.

B. A summary of the assembly profile of the F-BAR domain proteins. The times when the fluorescence signal appeared and disappeared at the CCP area are defined as "start" and "end," respectively, and are plotted (N = 20, for each condition). Time 0 was defined as the time when the clathrin signal disappeared. Statistical analysis was performed using Student's t-test, α = 0.05; ***: P < 0.001; ****: P < 0.0001. Error bars represent the standard deviation.

C. (Left) Time-lapse HS-AFM images obtained from Cos7 cells transfected with siRNA for CIP4, FBP17, or Synd2. The representative images are presented here. Additional cases are shown in Figure S2D. Images were taken every 10 s. Time 0 was defined as the time point when the pit completely closed on the HS-AFM image. The membrane bulge is indicated by arrowheads and the height information of the AFM image is presented using a color bar. Image size: 1.0 × 1.0 μm^2. (Right) The ratio of three different closing patterns in non-transfected Cos7 cells (N = 98) and the cells transfected with siRNA for the control (luciferase) (N = 60), CIP4 (N = 80), FBP17 (N = 60), or Synd2 (N = 60).

D. (Left) Correlative imaging of HS-AFM and CLSM. Cos7 cells expressing EGFP-fused CLTB and mCherry-fused CIP4 were imaged. Images were taken every 10 s. Time 0 was defined as the time point when the pit completely closed on the HS-AFM image. The membrane bulge is indicated by arrowheads and the height information of the AFM image is presented using a color bar. Image size: 1.0 × 1.0 μm^2. The representative images are presented here. Additional cases are shown in Figure S2F. (Right) A summary of the assembly profile of CIP4 and the membrane bulge formation. The time points when the membrane bulge and the fluorescence signal of CIP4 appeared and disappeared at the CCP area were defined as "start" and "end" points, respectively, and are plotted (N=16). Time 0 was defined as the time point of the complete pit closing and indicated with a black dotted line. Statistical analysis was performed using Student's t-test, α = 0.05; n.s., not significant (P > 0.05). Error bars represent the standard deviation.

E. Time-lapse superresolution SIM images obtained from Cos7 cells expressing EGFP-fused CLTB and mCherry-fused CIP4. Images were taken every second and displayed every 2 s. Image size: 0.5 × 0.5 μm^2. The fluorescent intensity of CIP4 and the x-y distance between the centroids of clathrin and CIP are plotted against time (bottom). Time 0 was defined as the time when the clathrin signal disappeared. The representative images are presented here. Additional cases are shown in Figure S2G.

F. The histogram of the x-y distance between the centroids of the clathrin and CIP4 fluorescence spots within the first 5 s of CIP4 assembly (N = 160, from 32 CMEs).

Please also refer to Figures S2 and S3.

128

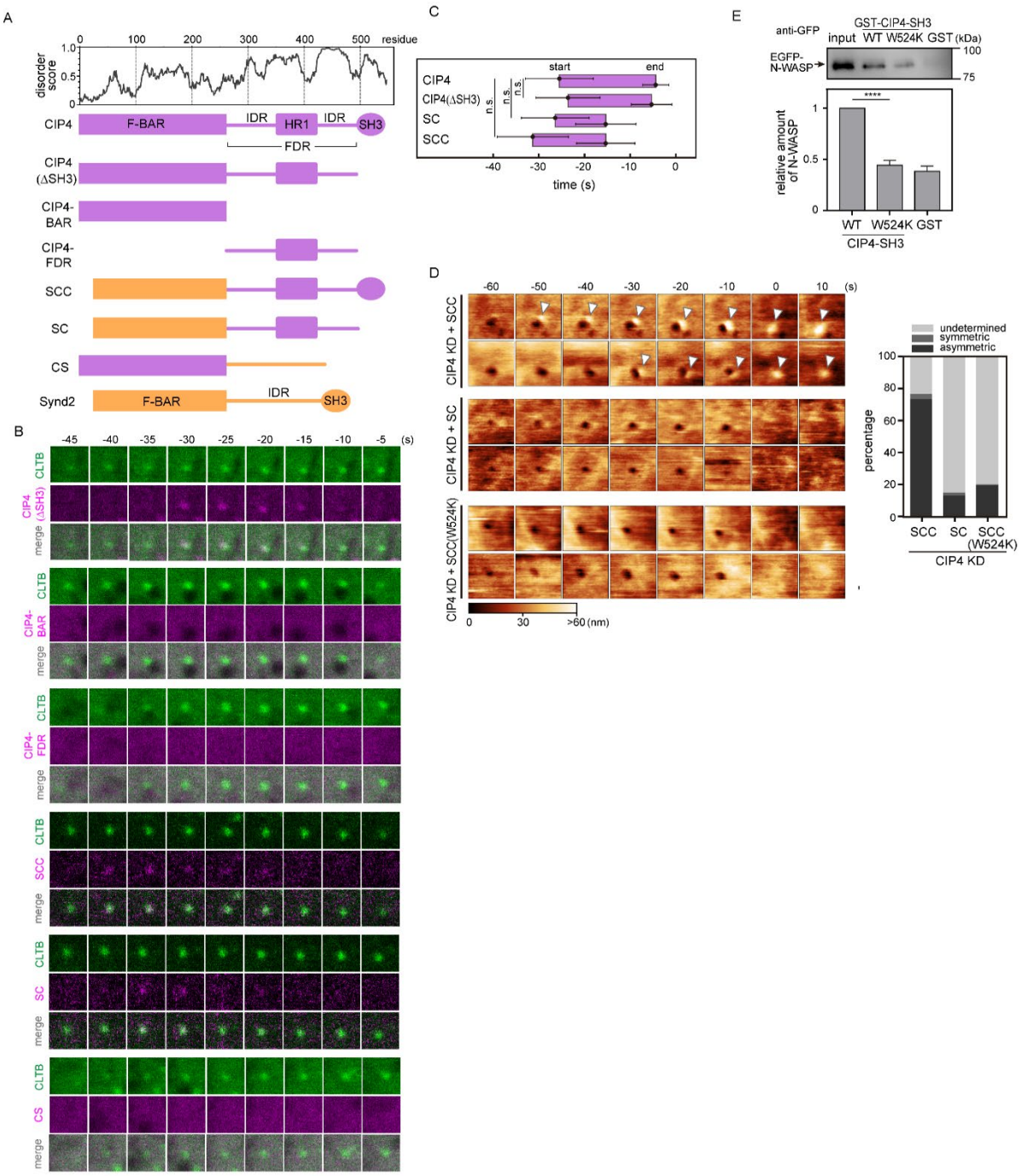

Flanking disordered region is necessary for the assembly of CIP4 to CCP

The domain of CIP4 that is required for its assembly around CCP was subsequently determined. CIP4 and FBP17 belong to the same subfamily of F-BAR proteins and have conserved F-BAR and SH3 domains at the amino- and carboxyl-termini, respectively (Figure S3D and E). The middle region between these conserved domains is less conserved and mostly disordered (Figure 3A and Figure S3D and E). In CIP4 and FBP17, but

Figure 3. Flanking disordered region (FDR) and SH3 domain is necessary for the asymmetric bulge.

A. (Top) Disorder plot of CIP4 predicted by IUPred. (Bottom) Schematic illustration of the domain structures of full-length CIP4 and Synd2, together with their chimeric constructs.

B. Time-lapse fluorescence images obtained from Cos7 cells expressing EGFP-fused CLTB and mCherry-fused CIP4 (WT or chimeric constructs). Image size: 1.0 × 1.0 μm^2. Time 0 was defined as the time when the clathrin signal disappeared. The representative images are presented here. Additional cases are shown in Figure S4A.

C. A summary of the assembly profile of CIP4, CIP4(ΔSH3), and chimeric molecules at CCP. Time 0 was defined as the time when the clathrin signal disappeared. The timing when the fluorescence signal appeared and disappeared at the CCP area was defined as "start" and "end," respectively, and are plotted (N = 20, for each condition). Statistical analysis was performed using Student's t-test, $\alpha = 0.05$; n.s., not significant ($P > 0.05$). The error bars represent the standard deviation.

D. Time-lapse HS-AFM images obtained from Cos7 cells expressing EGFP-fused SCC, SC, or SCC(W524K) mutants under the CIP4-KD background. The representative images are presented. Images were taken every 10 s. Time 0 was defined as the time point when the pit completely closed on the HS-AFM image. The membrane bulge is indicated by arrowheads and the height information of the AFM image is presented using a color bar. Image size: 1.0 × 1.0 μm^2. The frequency of three different closing patterns was measured and summarized in the right panel (N = 60, for each condition).

E. Pull-down assay of CIP4-SH3 and N-WASP. GST-tagged CIP4-SH3(WT) or CIP4-SH3(W524) was mixed with the HeLa cell lysate containing EGFP-fused N-WASP and GSH bead. The eluted fractions were analyzed using western blot with an anti-GFP antibody. The immunoreactive bands were quantified and summarized (bottom). Data are presented as mean ± standard deviation from three independent experiments as a relative value to WT. Statistical analysis was performed using Student's t-test, $\alpha = 0.05$; ****: $P < 0.0001$.

Please refer to Figure S3 and Figure S4.

not Synd2, the middle-disordered region is intervened by a conserved HR1 and therefore named the flanking-disordered region (FDR) (Figure 3A and Figure S3D).

The assembly of CIP4 at the CCP was not affected by the deletion of the SH3 domain (CIP4(ΔSH3) in Figure 3A–C, and Figure S4A). Neither the BAR domain nor the FDR by itself was sufficient for the assembly (Figure 3B), indicating that both the F-BAR domain and FDR are necessary for CIP4 to assemble at the CCP. Notably, the assembly of chimeric molecules carrying the Synd2-BAR and CIP4-FDR (SCC and SC chimera in Figure 3A) to the CCP starts at a similar time point to that of full-length CIP4 (Figure 3B and C and Figure S4A), whereas the CS mutant, which carries the CIP4-BAR and Synd2-IDR (Figure 3A), did not assemble at the CCP (Figure 3B). Together these results demonstrate that the FDR of CIP4 is a major determinant of the assembly at the CCP, although, the BAR domain is also necessary.

SH3 domain is required for the membrane bulge formation

In contrast to the assembly at the CCP, the SH3 domain was required for the formation of the membrane bulge. The expression of the SC chimera, which could assemble at the CCP (Figure 3B), failed to rescue the CIP4-knockdown (KD) phenotype; the frequency of the asymmetric membrane bulge was not recovered by the

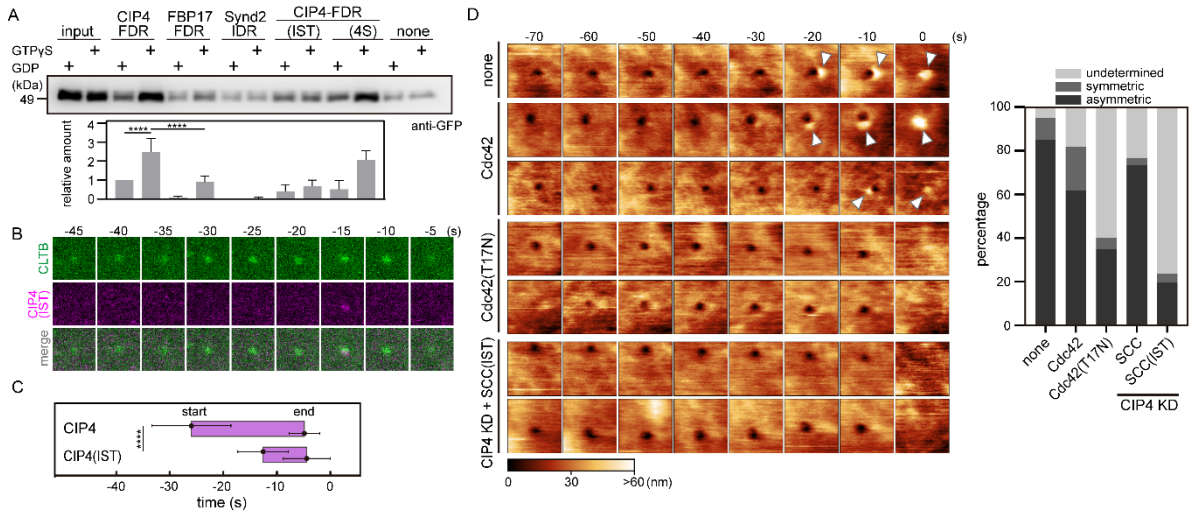

Figure 4. Interaction between Cdc42 and CIP4 is required for the asymmetric bulge.

A. Pull-down assay between Cdc42 and CIP4-FDR, FBP17-FDR, Synd2-IDR, CIP4-FDR(IST), or CIP4-FDR(4S) in the presence of GDP or GTP-γS. Hexa-histidine-tagged recombinant proteins were mixed with the cell lysate containing EGFP-fused Cdc42 in the presence of GDP or GTP-γS. The eluted fraction was subjected to the western blot analysis and is summarized in the bottom panel. Data are presented as mean ± standard deviation from three independent experiments as a relative value to the binding amount between CIP4-FDR and GDP-loaded Cdc42. Statistical analysis was performed using Student's t-test, $\alpha = 0.05$; ****: $P < 0.0001$.

B. Time-lapse fluorescence images of EGFP-fused CLTB and mCherry-fused CIP4 containing MGD to IST mutation expressed in Cos7 cells. Image size: 1.0 × 1.0 μm^2. Time 0 was defined as the time when the clathrin signal disappeared. The representative images are presented here. Additional cases are shown in Figure S5C.

C. A summary of the assembly profile of CIP4 and CIP4(IST) at CCPs. The timing when the fluorescence signal appeared and disappeared at the CCP area was defined as "start" and "end," respectively, and are plotted (N = 20, for each condition). Statistical analysis was performed using Student's t-test, $\alpha = 0.05$; ****: $P < 0.0001$. Error bars represent the standard deviation.

D. Time-lapse HS-AFM images obtained from Cos7 cells expressing EGFP (none), EGFP-fused Cdc42 (WT or T17N mutant), and the cells expressing EGFP-fused SCC(IST) under the CIP4-KD background. Representative images are presented. Images were taken every 10 s. Time 0 was defined as the time point when the pit completely closed on the HS-AFM image. The membrane bulge is indicated by arrowheads and the height information of the AFM image is presented using a color bar. Image size: 1.0 × 1.0 μm^2. The frequency of three different closing patterns was measured and summarized in the right panel (N = 60, for each condition).

Please also refer to Figure S5.

expression of the SC mutant (Figure 3D). In contrast, the SCC chimera, which also carries the SH3 domain of CIP4, could rescue the KD phenotype (Figure 3D), indicating that the SH3 domain was necessary for the formation of the membrane bulge after the assembly at the CCP.

CIP4 binds and activates N-WASP via the SH3 domain [38]. The activated N-WASP interacts with Cdc42 through its GTPase binding domain (GBD) (Figure S4B and C) and recruits the Arp2/3 complex to promote actin polymerization [39]. In our experimental system, the assembly of N-WASP at the CCP was also observed; it appeared at the CCP immediately after CIP4 (Figure S4D and E). Therefore, we examined whether the interaction between CIP4 and N-WASP is necessary for the asymmetric bulge. A point mutation in the SH3

157 domain of Toca1 (W518K) inhibited the interaction with N-WASP [40]. Mutating the corresponding residue in
158 the CIP4-SH3 domain (W524K) also reduced the interaction with N-WASP (Figure 3E and Figure S4F). In
159 agreement with this, the SCC chimera carrying the W524K mutation failed to rescue the CIP4-KD phenotype
160 (Figure 3D), indicating that the interaction with CIP4-SH3 and N-WASP is necessary for the formation of the
161 asymmetric bulge.
162

163 **Cdc42 recruits CIP4 to the site of CCP**

164 Next, we examined the involvement of FDR in the asymmetric assembly of CIP4 at the CCP. We first focused
165 on the interaction with Cdc42 [41,42]. A pull-down assay demonstrated that the CIP4-FDR had a higher affinity to
166 the active (GTPγS-loaded) form of Cdc42 than the FBP17-FDR and the IDR of Synd2 (Figure 4A, and Figure
167 S5A). Substitutions of three amino acids within HR1 (MGD to IST, Figure S5B), which abolish the interaction
168 with Cdc42 in Toca1-HR1 [40], also attenuated the interaction with Cdc42 (Figure 4A, and Figure S5A). The
169 assembly of full-length CIP4 carrying MGD-IST mutations at the CCP started at -12.5 ± 5.2 s (Figure 4B and
170 C and Figure S5C), which was delayed compared to that of the wild type (WT), indicating that the activated
171 Cdc42 is required for the assembly of CIP4 to the CCP.

172 The interaction with active Cdc42 was important not only for the assembly at the CCP but also for
173 the asymmetric bulge formation. The overexpression of a dominant-negative form of Cdc42(T17N), but not the
174 WT, severely impaired the asymmetric bulge (to ~17%) (Figure 4D). In addition, the SCC chimera carrying the
175 MGD-IST mutation failed to rescue the phenotype of CIP4-KD (Figure 4D). These results indicated that
176 activated Cdc42 recruits CIP4 to the site of CCP which further induces the formation of the asymmetric bulge.
177

178 **Self-assembly of FDR generates the "asymmetric" distribution of CIP4**

179 Although the interaction between Cdc42 and CIP4 plays a role in the assembly of CIP4 at the CCP, it does not
180 explain how "asymmetricity" is produced. One of the possible mechanisms could be the cooperativity of the
181 assembly. The structural prediction based on the amino-acid sequence suggested that the HR1 of CIP4 forms a
182 helical coil that is composed of two antiparallel α-helices (Figure S6A). The circular dichroism spectrum
183 measurement of the recombinant HR1 indeed exhibited a strong propensity of α-helix (Figure S6B). Therefore,
184 we speculated that it forms a multimer and the association proceeds with cooperativity. To test this, recombinant

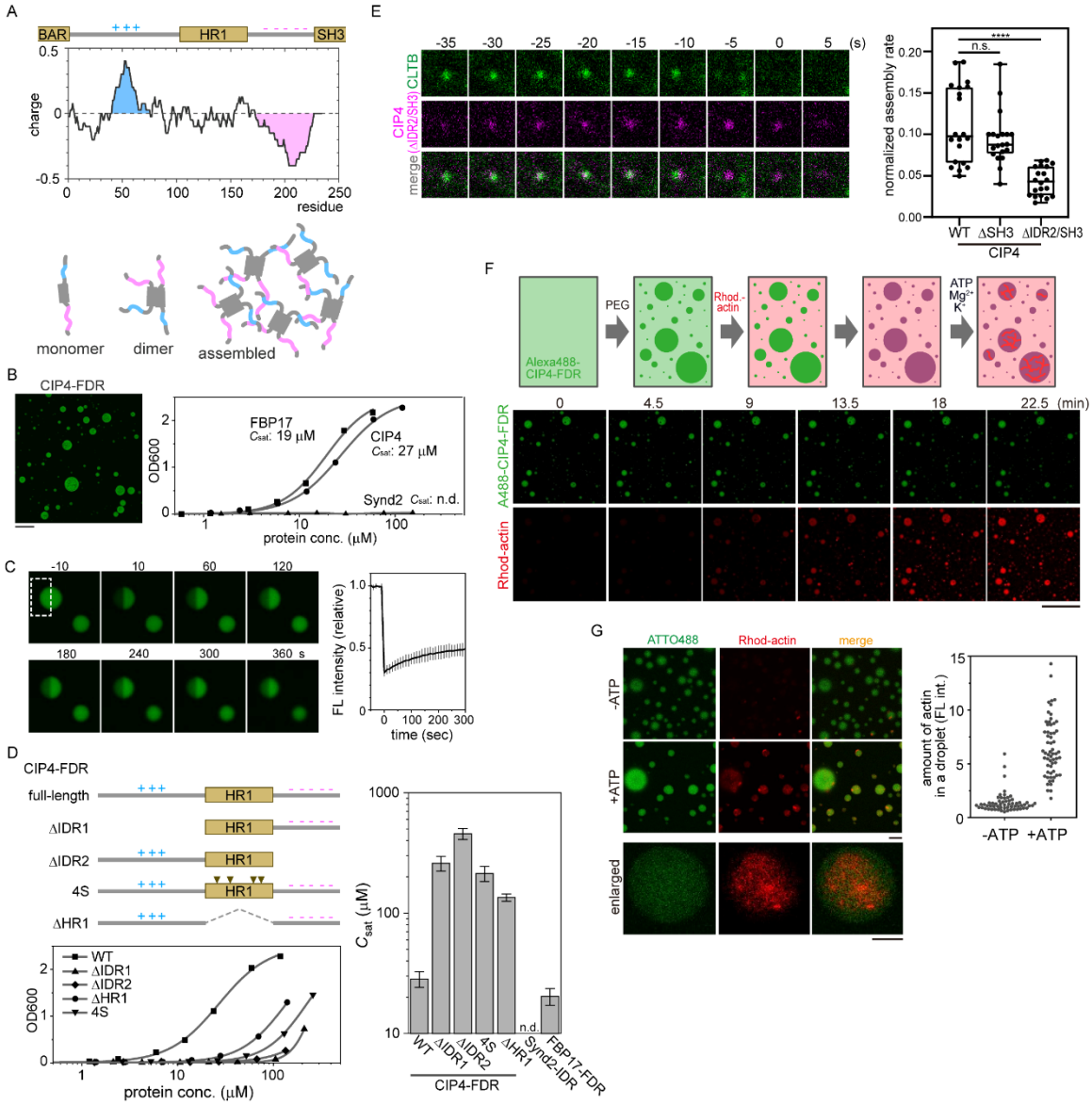

185 HR1 was purified and its molecular size was estimated using gel filtration chromatography. HR1 existed mainly
186 as a dimer (Figure S6C and D) and any multimers could not be detected in a physiological condition,
187 demonstrating that HR1 multimerization is not the major driving force of asymmetricity.

188 Another possibility could be a self-assembly and phase transition of FDR via electrostatic interaction
189 between IDRs. The HR1 domain of CIP4 and FBP17 is flanked by positively and negatively charged IDRs at
190 the amino and carboxyl sides, respectively (Figure 5A and Figure S6E). In contrast, the charge segregation of
191 Synd2 IDR was not so prominent (Figure S6E). It has been well-established that a polymer with segregated
192 charges (i.e., block polyampholyte) exhibits stronger liquid-liquid phase separation (LLPS) than the chain with
193 the same number of charges randomly distributed (i.e., random polyampholyte) [43-45]. These properties strongly

Figure 5. CIP4-FDR phase separates and promotes actin polymerization.

A. (Top) A charge plot of CIP4-FDR. HR1 is flanked by a net positive (marked in blue) and negative (marked in red) IDRs. (Bottom) A schematic illustration of phase separation of CIP4-FDR driven by electrostatic interaction between IDRs and HR1 dimerization.

B. *In vitro* phase separation of FDRs from CIP4 and FBP17 and IDR from Synd2. CIP4-FDR, Synd2-IDR, and FBP17-FDR were purified from bacteria, and incubated with 15 % polyethylene glycol. The turbidity of the solution was measured based on optical density at 600 nm, and plotted against the protein concentration. The saturation concentration (C_{sat}) was obtained by curve fitting (Methods) and is indicated. A representative microscopic image of the droplet of CIP4-FDR is also shown. For fluorescence imaging, protein was pre-labeled with ATTO488. Scale bar, 50 μm.

C. FRAP analysis of a protein droplet formed by CIP4-FDR. The protein droplet of ATTO488-labeled CIP4-FDR was prepared as shown in B. Half of the target droplet (dotted square) was bleached by laser radiation, and time-lapse imaging was continued every 10 s. Some representative images are shown. The average fluorescence intensity of the bleached region was quantified and plotted against time as a relative value to that of the pre-bleached signal. Data are presented as mean ± standard deviation from 5 independent measurements.

D. (left top) A schematic illustration of CIP4-FDR and its deletion mutants. (left bottom) The turbidity assay was performed and plotted as described in (B). (right) The C_{sat} values obtained from a series of turbidity assays are summarized. Data are presented as mean ± standard deviation from three independent experiments.

E. (Left) Time-lapse fluorescence images of EGFP-fused CLTB and mCherry-fused CIP4(ΔIDR2/SH3) expressed in Cos7 cells. Image size: 1.0 × 1.0 μm^2. Time 0 was defined as the time when the clathrin signal disappeared. The representative images are presented here. Additional cases are shown in Figure S6F. (Right) Assembly rates of CIP4 (WT, ΔSH3, and ΔIDR2/SH3) at CCPs was plotted (N = 20, for each condition). The median, lower quartile, and upper quartile values are shown in the box and the minimum and maximum values are indicated with upper and lower whiskers, respectively. Statistical analysis was performed using the Student's t-test, $\alpha = 0.05$; ****: $P < 0.0001$; n.s., not significant ($P > 0.05$).

F. (Top) A schematic illustration of actin polymerization in a protein droplet of CIP4-FDR. After forming a droplet of ATTO488-labeled CIP4-FDR, rhodamine-labeled G-actin was incubated with ATP, Mg^{2+}, and K^+. (Bottom) Time-lapse fluorescence observation of CIP4-FDR (ATTO488-labeled) and G-actin (rhodamine-labeled). Scale bar, 100 μm.

G. (Left) A mixture of rhodamine-labeled and non-labeled G-actin (1:9) was loaded with or without ATP and $Mg^{2+,}$ and incubated with pre-formed droplet of CIP4-FDR. Representative fluorescence images are shown. Enlarged images in the presence of ATP are shown below. (Right) Fluorescence intensity of F-actin in the droplet was quantified and plotted (N = 60, in each condition).

Please also refer to Figure S6.

194 suggest that the FDR self-assembles to undergo LLPS via electrostatic interaction among IDRs (Figure 5A). To
195 test this possibility, the recombinant protein of CIP4-FDR and FBP17-IDR was purified and subjected to an *in*
196 *vitro* droplet assay in the presence of polyethylene glycol as a crowder. As shown in Figure 5B, CIP4-FDR
197 formed protein droplets, unlike the IDR of Synd2. Quantification of protein droplets based on the turbidity
198 revealed that the saturation concentration of CIP4-FDR was similar to that of the FBP17-FDR, but was
199 remarkably lower than that of the Synd2-IDR (Figure 5B), indicating that CIP4-FDR and FBP17-FDR has a
200 stronger propensity for LLPS than Synd2-IDR. Fluorescence recovery after photobleaching (FRAP) analysis
201 revealed that the protein droplet was in a liquid-like state (Figure 5C). Deletion of either IDR (ΔIDR1 or ΔIDR2)
202 from CIP4-FDR severely attenuated the LLPS (Figure 5D), demonstrating that the interaction between positive
203 and negative IDRs plays a role in the LLPS of FDR.

204 The deletion of HR1 from FDR (ΔHR1) also reduced the propensity of LLPS (Figure 5D), implying
205 the involvement of HR1-dimerization in the LLPS. To confirm this, intensive mutations were introduced into
206 HR1 to reduce dimer formation. We found that substitutions of four hydrophobic residues (L347, L401, Y408,
207 and W411 labeled in Figure S6A) by serine (4S) disrupted the HR1-dimer without affecting the interaction with
208 Cdc42 (Figure 4A, Figure S5A, and Figure S6C). As expected, LLPS propensity of the CIP4-FDR(4S) mutant
209 was lower than that of the WT (Figure 5D), indicating that HR1 dimerization promotes the FDR-dependent
210 assembly of CIP4.

211 To test whether FDR-driven LLPS plays a role in the assembly of CIP4 at the CCP *in vivo*, we analyzed
212 the assembly rate of CIP4 through live-cell fluorescence imaging. The assembly rate of CIP4(ΔSH3) at the CCP
213 was comparable to that of the full-length (Figure 5E). In contrast, further deletion of IDR2(ΔIDR2/SH3) reduced
214 the assembly rate by ~70 % (Figure 5E and Figure S6F), indicating that IDR2 plays a critical role in CIP4
215 assembly. Similarly, the 4S mutation in the full-length CIP4 almost completely abolished the assembly (Figure
216 S6G), which was more severe than the deletion of IDR2. In agreement with this, the SCC chimera carrying the
217 4S mutation failed to rescue the CIP4-KD (Figure S6H). These observations indicated that the FDR-dependent
218 LLPS plays a critical role in the assembly of CIP4 at the CCP *in vivo*.

219

220 **Actin accumulates and polymerizes in a liquid phase of CIP4-FDR**

221 We then examined whether a liquid phase formed by CIP4-FDR can accelerate actin polymerization. Alexa488-
222 labeled CIP4-FDR was mixed with polyethylene glycol to induce LLPS, and then rhodamine-labeled G-actin
223 was added (Figure 5F). The time-lapse observation under a fluorescence microscope revealed that actin rapidly
224 moved into the droplet (Figure 5F). The concentration of actin reached ~100 times higher in the droplet than
225 that in the external medium, demonstrating that actin accumulated in the droplet of CIP4-FDR.

226 We then tested whether actin polymerization also occurs in the droplet. To induce actin polymerization
227 in the droplet, ATP and Mg^{2+} and a low concentration of G-actin (45 μg/mL) were added to the droplet solution
228 of CIP4-FDR (Figure 5F and G). Under this condition, action polymerization rarely occurred in the diluted
229 phase, owing to the low concentration of actin. However, fibrous actin was frequently observed in the droplet
230 (Figure 5G). The depletion of ATP almost completely abolished it (Figure 5G), demonstrating that actin

231 polymerization occurs in the droplet. Together, these results demonstrated that CIP4 not only self-assembles
232 via FDR to form a liquid-like phase but also concentrates G-actin in the liquid phase to accelerate the
233 polymerization.
234

235 # Discussion

236 Herein, we used various live-cell imaging techniques and biochemical approaches to demonstrate that the BAR
237 domain-containing protein, CIP4, plays a critical role in the actin-dependent asymmetric closing process of
238 CME. CIP4 interacts with curved-membrane and actin-related proteins such as Cdc42 and N-WASP through its
239 distinct structured domains (i.e., BAR, HR1, and SH3). Our results demonstrated that the asymmetricity was
240 generated during the self-assembly of the disordered regions between those structured domains. This describes
241 an intriguing molecular mechanism of how a multi-domain protein, such as CIP4, spatio-temporally recruits
242 and orchestrates the actin machinery at a specific position of the cell. Strong self-assembly and phase separation
243 of IDRs, together with stereospecific interactions between structured domains, induces a local burst of branched
244 actin fibers nearby the CCP. The IDRs of membrane-bound, -anchored, and -embedded proteins are gaining
245 more attention for their effects on curvature sensing and membrane bending. Several endocytic proteins
246 including AP180, Amphiphysin 1, and FBP17 can sense a membrane curvature via their disordered regions [46-
247 48]. Current assumptions suggest that disordered regions can sense the curved lipid bilayer by either entropic or
248 electrostatic mechanisms that were determined by the length and net charge of the disordered chains [49]. A
249 common strategy applied by disordered proteins, including BAR domain proteins, to curve the membrane is
250 domain crowding or phase separation, which imposes intense compressive or steric pressure on the flat lipid
251 bilayer [50-53]. Together, these findings provide a novel perspective for understanding the role of disordered
252 proteins in CME progression.
253

254 **Structural and functional diversity of F-BAR domain-containing proteins**

255 There are four members of F-BAR domain-containing proteins: CIP4, FBP17, Synd2, and Toca1. CIP4, FBP-
256 17, and Synd2 assemble at the CCP at different times during CME (Figure 2B) and have different cellular
257 functions [54,55] despite their similar domain structures. This could partly be attributed to the slightly different

258 curvature of the 3D structures of the BAR domains [35]. Herein, we demonstrated that the middle disordered
259 regions lying between the BAR and SH3 domains had different properties of self-assembly. The FDRs of CIP4
260 and FBP17, but not the IDR of Synd2, had high propensities of LLPS, which was a result of different charge
261 distributions and the presence of the HR1 domain (Figure 5A and Figure S6E). These results clearly explain the
262 functional diversity between Synd2 and CIP4 and FBP17 in CME and possibly other cellular processes in which
263 they are involved.

264 In contrast to Synd2, the FBP17-FDR has a similar charge distribution pattern to that of CIP4 (Figure
265 S6E) and exhibits a similar phase behavior *in vitro* (Figure 5B); however, they greatly diverge regarding their
266 *in vivo* functions and localizations. During CME, CIP4 assembles at the CCP before complete pit-closure which
267 is remarkably earlier than that of FBP17 (Figure 2B and D). Although the HR1 domains of CIP4 and FBP17
268 have a similar affinity to Cdc42 [56], *in vitro* pull-down assay revealed that the FDR of CIP4 had a higher affinity
269 to Cdc42 (Figure 4A and Figure S5A); this implies that disordered regions have a role in Cdc42 interactions. In
270 dendritic neurons, FBP17 showed a different intracellular distribution from that of CIP4 due to its poly PxxP
271 region within the first IDR [57]. These observations implicate an underestimated role of disordered regions in
272 regulating nearby stereospecific interactions.

273

274 **Phase separation of IDR and stereo-specific interactions coordinate to produce an asymmetric**
275 **distribution of actin machinery**

276 Although the FDR of CIP4 strongly self-assembled and underwent LLPS *in vitro* (Figure 5B), it did not
277 condensate by itself even under *in vivo* overexpression (Figure 3B). These results imply that other domains and
278 interactions define the spatio-temporal assembly of CIP4 at the CCP. CIP4 contains several structural domains:
279 BAR domain for interacting with the membrane, HR1 for interacting with activated Cdc42, and SH3 domain
280 for N-WASP (Figure 3E and Figure S4B, C, and F). Our results demonstrate that stereo-specific interactions of
281 these structured domains play critical roles in locating the CIP4 near the CCP and in recruiting actin-related
282 machinery.

283 In the absence of the CCP, CIP4 binds to membrane-anchored active Cdc42 via the HR1 domain [58-60]
284 (Figure 6A). CIP4 also binds to N-WASP via the SH3 domain and disables the auto-inhibition of N-WASP to
285 allow the interaction with Cdc42 via the GBD, and ternary complexes form among CIP4, N-WASP, and Cdc42

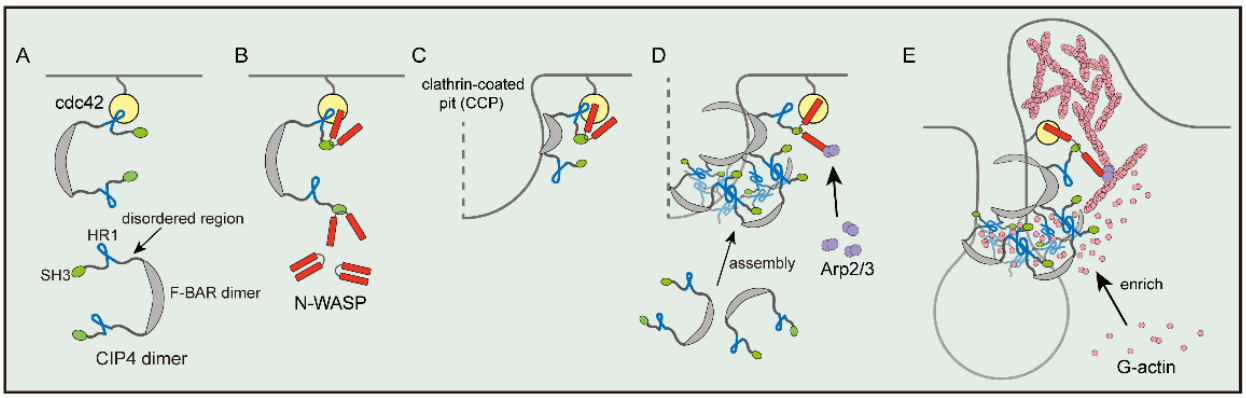

Figure 6. CIP4 drives the asymmetric CCP closing.

A–E. Schematic illustrations of the CIP4-induced asymmetric CCP closing. Membrane-bound and activated Cdc42 recruits CIP4 via direct interaction with HR1 (A). CIP4 then recruits and activates N-WASP to form a ternary complex (B). When the membrane-bound complex gets close to a CCP, the F-BAR domain of CIP4 recognizes and assembles on the curved membrane (C). This increases the chance of interaction between FDRs and initiates phase separation, which results in an asymmetric assembly nearby the CCP (D). Meanwhile, activated N-WASP further recruits and activates the Arp2/3 complex which initiates actin polymerization (D). The condensed phase of CIP4-FDR concentrates G-actin and accelerates the local actin polymerization which creates an actin-rich environment (E). As a result, polymerized actin accumulated rapidly and asymmetrically around CCP which deforms the plasma membrane and promotes the complete closing of CCP (E).

286 (Figure 6B). However, at this stage, the local concentration of CIP4 may not be high enough to undergo LLPS
287 (Figure 6B). When the ternary complex gets close to the CCP, the BAR domain recognizes the membrane
288 curvature of the pit and binds to it (Figure 6C). Although the BAR domain is known to multimerize on the
289 membrane *in vitro* [61], it was not sufficient for assembly at the CCP, and the FDR was also necessary (Figure 3B
290 and Figure S4A). These results imply that both the self-assembly of FDR and the multimerization of the BAR
291 domain on the membrane synergistically work for the fast assembly of CIP4 at the CCP. This is in good
292 agreement with the previous study demonstrating that disordered domains enhance the affinity of BAR domains
293 to the curved membrane [46]. Moreover, our chimeric molecule between CIP4 and Synd2 demonstrated that the
294 BAR domain was functionally exchangeable (SCC chimera, Figure 3A–C and Figure S4A), implying that the
295 curvature-sensing by the BAR domain may not be critical at this step of the CME. The SH3 domain was not
296 necessary for the assembly of CIP4 (Figure 3A–C and Figure S4A), although it is necessary for recruiting N-
297 WASP and subsequent formation of the asymmetric bulge (see later section).

298 Upon CIP4 self-assembly initiation, the local concentration of CIP4 at a specific position near the CCP
299 rapidly increases (Figure 6D). Compared to HR1, GBD has a higher affinity to Cdc42 and will completely
300 displace the HR1 to interact with Cdc42, which further exposes the C-terminal acidic region of N-WASP

301 allowing the further recruitment and activation of the Arp2/3 complex [56]. As a result, the local concentration of
302 the active Arp2/3 complex also increases, which accelerates actin polymerization (Figure 6D and E). A similar
303 process had been demonstrated using Toca1, a subfamily member of CIP4 with a conserved HR1 and SH3
304 domain [40,56,62], suggesting a conserved role of CIP4 sub-family proteins in mediating Cdc42-WASP-Arp2/3
305 actin signaling. In addition to Arp2/3 complex accumulation, our *in vitro* assay demonstrated that G-actin
306 preferred to localize in the condensed phase of CIP4-FDR (Figure 5F and G), implying that the concentration
307 of free G-actin increases in the CIP4-rich phase near the CCP, which also promotes actin polymerization. A
308 recent study revealed that actin-associated proteins with a long IDR, such as vasodilator-stimulated
309 phosphoprotein and actin-binding LIM protein 1, formed liquid droplets under physiological conditions and
310 promoted actin polymerization and bundling [63,64]. It is hypothesized that LLPS is an effective method applied
311 by actin-related proteins to regulate the actin cytoskeleton.

312 It was recently reported that CIP4 is enriched at the site of artificially-induced nano-scale membrane
313 invaginations, induces actin polymerization in a Cdc42-dependent pathway, and that disordered proteins were
314 proven to sense the membrane curvature outside the area of endocytosis, such as in filopodia [46,58]. Therefore, it
315 is reasonable to believe that the reorganization of the actin cytoskeleton through F-BAR domain proteins plays
316 a critical role in a variety of cellular structures of the curved membrane, and this should be further elucidated.

317

318 ## Data and code availability

319 This study includes no original code deposited in external repositories. All original data will be deposited at
320 Mendeley Data before the acceptance of this manuscript (Reserved DOI: 10.17632/xt2prdpnw7.1). Any
321 additional information required to reanalyze the data reported in this study is available from the lead contact
322 (RL) upon request

323

324 ## Acknowledgments

325 We thank K. Deguchi, S. Dodo, and B. Yi at Kyoto University for their technical assistance. We are especially
326 thankful to Dr. F. Ishidate at the iCeMS Analysis Center, Institute for Integrated Cell-Material Sciences (WPI-
327 iCeMS), Kyoto University Institute for Advanced Study (KUIAS) for his technical assistance in super-

resolution structural illumination microscopy (Elyra 7). We also thank Mr. Sakai, Mr. Uekusa, Mr. Yagi, and Mr. Ito for their assistance in constructing and maintaining the HS-AFM system. This work was supported by JSPS KAKENHI Grant Numbers JP18H02436, JP18KK0196, JP19K22422, and JP22H05171 for SHY, and AMED (Japan Agency for Medical Research and Development) under Grant Number JP18gm5810018 and JP20wm0325009 for SHY.

Author contributions

Research design: Yiming Yu, Shige H. Yoshimura; Experiment and data analysis: Yiming Yu, Ozaki Takuma, Shige H. Yoshimura; Manuscript writing: Yiming Yu, Shige H. Yoshimura.

Conflict of interest

The authors declare that they have no conflict of interest.

STAR Methods

Plasmids

Mammalian expression vectors encoding pEGFP-N1-CLTB and pmCherry-C1-CLTB were constructed as described previously [30]. Fragments of the full-length (FL) CIP4 (amino acids (a.a.) 1 – 547), FL-FBP17 (a.a. 1 – 617), FL-Synd2 (a.a. 1 – 486), CIP4-F-BAR (a.a. 1 – 257), CIP4-FDR (a.a. 258 – 489), CIP4(ΔSH3) (a.a. 1 – 489), and CIP4(ΔIDR2/SH3) (a.a. 1 – 425) were amplified by PCR and subcloned into pmCherry-C1 vectors for mammalian expression. Fragments of CIP4-FDR (a.a. 258 – 489), FBP17-FDR (a.a. 258 – 552), Synd2-IDR (a.a. 276 – 428), CIP4-FDR-ΔIDR1 (a.a. 339 – 489), CIP4-FDR-ΔIDR2 (a.a. 258 – 425), CIP4-HR1 (a.a. 339 – 425), CIP4-SH3 (a.a. 490 – 547), and N-WASP-GBD (a.a. 197 – 255) were amplified by PCR and subcloned into pET28a (+) or pGEX-6P-1 vectors for expression in *Escherichia coli*.

Vectors encoding mCherry-fused and EGFP-fused CSS chimeric molecules were constructed by amplifying and ligating the DNA fragments corresponding to CIP4 (a.a. 1 – 257) and Synd2 (a.a. 276 – 486) and subcloning into pEGFP-C1 and pmCherry-C1 vectors. Similarly, fragment of SCC chimera were obtained by amplifying and ligating the nucleotide sequence corresponding to Synd2 (a.a. 1 – 275) and CIP4 (a.a. 258 – 547). To obtain

355 the fragments of SC and CS chimera, the DNA fragments corresponding to CIP4-SH3 (a.a. 490 – 547) and
356 Synd2-SH3 (a.a. 429 – 486) were deleted from the SCC or CSS fragments respectively by PrimerSTAR® Max
357 DNA Polymerase (Takara Bio Inc., Shiga, Japan). Fragment of CIP4-FDR(ΔHR1) was obtained by deleting the
358 nucleotide sequence corresponding to CIP4-HR1 (a.a. 339 – 425) by PrimerSTAR® Max DNA Polymerase.
359 Single and multiple amino acid mutations were introduced using PrimerSTAR® Max DNA Polymerase. The
360 MGD to IST mutation was generated by replacing the amino acids of M381, G382, and D383 with I, S, and T,
361 respectively; the 4S mutation was generated by replacing the amino acids of L347, L401, Y408, and W411 with
362 S; the W524K mutation was generated by replacing the amino acids of W524 with K.
363 Fragments of the Cdc42 (a.a. 1 – 191) and N-WASP (a.a. 1 – 511) were amplified by PCR and subcloned into
364 pEGFP-C1 vectors for mammalian expression. pcDNA3-EGFP-Cdc42(T17N) was obtained from Klaus Hahn
365 (Addgene; plasmid # 12601) [65].
366
367 ***Expression and purification of recombinant proteins***
368 The following recombinant proteins were used herein: hexa-histidine-tagged CIP4-FDR, FBP17-FDR, Synd2-
369 IDR, CIP4-FDR(4S), CIP4-FDR(IST), CIP4-HR1, CIP4-HR1(4S), CIP4-FDR(ΔHR1), CIP4-FDR(ΔIDR1) and
370 CIP4-FDR(ΔIDR2), and glutathione S-transferase (GST)-tagged CIP4-SH3, CIP4-SH3(W524K), and N-
371 WASP-GBD. Vectors encoding the recombinant proteins were constructed as described in the previous section
372 and introduced into the BL21-CondonPlus (DE3)-RIL competent cells (Agilent Technologies, Inc., Santa Clara,
373 CA, USA) by heat shock at 37 °C for 30 s. The expression of the recombinant protein was induced by 0.5 mM
374 isopropylthio-β-D-galactoside at 16 °C for 16 h. Bacterial cells expressing hexa-histidine-tagged or GST-tagged
375 recombinant proteins were harvested and resuspended with phosphate buffered saline (PBS) (137 mM NaCl,
376 2.7 mM KCl, 10 mM Na_2HPO_4, and 1.8 mM KH_2PO_4) (pH 7.4) containing lysozyme (0.2 mg/mL), DNaseI (20
377 μg/mL), $MgCl_2$ (1 mM), and phenylmethanesulfonylfluoride (1 mM). The cells were subjected to freeze-thaw
378 cycles three times and homogenized by sonication. Insoluble cell debris was removed by centrifugation at
379 12,000 rpm, 4 °C for 15 min. To collect tagged proteins, the cleared lysate was then mixed with nickel-
380 nitrilotriacetic acid (Ni-NTA)-agarose beads (QIAGEN, Hilden, Germany) or glutathione (GSH) Sepharose 4B
381 beads (Cytiva, Marlborough, MA, USA), and incubated at 4 °C for 1 h with rotation. The hexa-histidine- and

382 GST-tagged proteins were eluted with Elution buffer A (100 mM NaCl, 50 mM HEPES, 0.2 mM DTT, 400
383 mM Imidazole, pH 7.4), and Elution buffer B (100 mM NaCl, 50 mM HEPES, 0.2 mM DTT, 200 mM GSH,
384 pH 7.4), respectively, and dialyzed against a buffer containing 200 mM NaCl and 50 mM HEPES (pH 7.4) at
385 4 °C for 6 h. Proteins were concentrated by AmiconUltra (M.W. 3,000 Da) (Sigma-Aldrich, St. Louis, MO,
386 USA) and stored at -80 °C before use.
387
388 ***Pulldown assay***
389 The recombinant proteins (~5 μg) were immobilized on ~20 μl of Ni-NTA agarose or GSH beads. EGFP-fused
390 Cdc42 and EGFP-fused N-WASP were expressed in HEK293T cells. The cell pellet was resuspended with PBS
391 containing Protease Inhibitor Cocktail (0.5 %, Nacalai Tesque, Inc., Kyoto, Japan) and Triton-X-100 (0.25 %)
392 on ice for 10 min. To activate Cdc42, the cell lysate containing EGFP-Cdc42 (WT or T17N) was incubated with
393 GTPγ-S or GDP as described previously [66]. The cell lysate was mixed with the purified recombinant protein and
394 Ni-NTA or GSH beads and incubated at 4 °C for 25 min and the bound fraction was eluted with 400 mM
395 Imidazole or 100 mM GSH) in Elution Buffer (100 mM NaCl, 50 mM HEPES, 0.2 mM DTT, pH 7.4),
396 respectively. Approximately 20 % of the bound fraction and ~ 10 % of the unbound fraction were analyzed
397 using immunoblotting and SDS-PAGE, respectively.
398
399 ***Cell culture and transfection***
400 Monkey kidney-dived fibroblast-like cells (Cos7 cells) purchased from the Cell Engineering Division in RIKEN
401 BioResource Center (RBC0539; Ibaraki, Japan) were cultured in high-glucose Dulbecco's Modified Eagle
402 Medium (DMEM) supplemented with 10 % fetal bovine serum (FBS) at 37 ℃ with 5 % CO_2. For HS-AFM
403 observation, slide glasses (Matsunami Glass Ind., Ltd., Osaka, Japan) or 0.15 CG pierced slide glass (ToA
404 Optical Technologies, Inc., Tokyo, Japan) were coated with 0.01 % poly-L-lysine solution (Sigma-Aldrich) and
405 incubated at 37 ℃ for 1 h. Cos7 cells were seeded on the glass, incubated overnight, and subjected to HS-AFM
406 observation the next day. CK666 (Abcam, Cambridge, United Kingdom) was added to the culture medium to a
407 final concentration of 100 μM 30 min before the observation. Polyethyleneimine (M.W. 40,000, Polycience,
408 Niles, IL, USA) was used to introduce the expression vectors into Cos7 cells.

409

410 ***RNA interference***

411 Cos7 cells were transfected with siRNA using HiPerfect reagent (QIAGEN) according to the manufacturer's
412 protocol. siRNA against CIP4 (ID: s17814, 5′-GGAGAAUAGUAAGCGUAAATT-3′), against FBP17 (ID:
413 s22916, 5′-CAACCUAAAAAGAACUCGATT-3′), or against Synd2 (ID: s22216, 5′-
414 AGAUGUUCUUAAGACCAAATT-3′) were purchased from Ambion Inc. (Austin, TX, USA). siRNA against
415 N-WASP (siGENOME SMART pool) was purchased from Dharmacon Inc. (Lafayette, CO, USA). The cells
416 were treated with trypsin 48 h after the transfection and seeded on slide glasses for HS-AFM observation or
417 directed harvested and analyzed using SDS-PAGE followed by immunoblotting. The rescue experiment was
418 performed by transfecting Cos7 cells with siRNA against CIP4 48 h before the observation and transfecting the
419 cells with vectors encoding mCherry-tagged SC chimera 24 h before the observation.

420

421 ***HS-AFM imaging and image analyses***

422 A tip-scan type HS-AFM system (BIXAM^{TM}; Olympus Corporation, Tokyo, Japan) combined with confocal
423 microscope (FV1200, Olympus Corporation) [30,67,68] was used for AFM imaging. All observations were
424 performed at 28 °C. An electron beam-deposited ultra-short cantilever (USC-F0.8-K0.1-T12-x66-10;
425 Nonoworld Corporation, Neuchâtel, Switzerland) with a spring constant of 0.1 N m^{-1} was used for scanning.
426 The scanning speed was 10 s per frame, and the total scanning area was 6000 × 4500 nm^2. A correlative imaging
427 of HS-AFM and confocal microscopy was performed as described previously [30].

428 Time-lapse HS-AFM images were acquired using AFM Scanning System Software Version 1.6.0.12
429 (Olympus Corporation). The diameter, duration, and height of the membrane bulge were analyzed by using
430 Gwyddion software (ver 2.55) (http://gwyddion.net/) and GIMP software (ver 2.10.18) (https://www.gimp.org/).
431 To record the height of the membrane bulge, the highest point of the plasma membrane at the CCP area was
432 recorded and compared with the surrounding plasma membrane. The lowest position in the HS-AFM image
433 was set as '0' automatically. The duration of the membrane bulge was counted from the first image with the
434 observable membrane bulge to its complete disappearance. For the size of the pit, the maximum diameter of the
435 pit during the whole process of CME was measured by first doing a cross-section and measuring the distance
436 between one side of the pit to the other side. For cases with no detectable membrane bulge (undetermined

437 pattern), the height and duration were set as '0 μm' and '0 s' respectively. By plotting the change of membrane
438 height at the pit area and pit diameter against time, the slope of the ascending part of the height-time plot was
439 used to obtain the growth rate of the membrane bulge while the slope of the descending part of the diameter-
440 time plot was used to obtain the closing rate of CCPs.
441
442 ***Immunoblotting***
443 The total cell lysate from Cos7 cells expressing EGFP-fused CIP4, FBP17, or Synd2 and from Cos7 cells
444 subjected to single KD of CIP4, FBP17, or Synd2 was separated by 12 % SDS-PAGE gel, transferred to a poly
445 vinylidene difluoride membrane, blocked in 5 % slim milk in tris buffered saline (5 mM Tris, 13.8 mM NaCl,
446 0.27 mM KCl, pH 7.4) containing 0.1 % Tween (Nacalai Tesque, Inc.), and incubated with a primary antibody
447 for 1 h. The following antibodies were used: rabbit anti-CIP4 (1:1000; Bethyl Laboratories Inc., Montgomery,
448 TX, USA), rabbit anti-pacsin2 (1:1000; Novusbio), rabbit anti-FNBP1 (1:1000; Novus Biologicals LLC,
449 Centennial, CO, USA), rabbit anti-N-WASP (1:1000; Cell Signaling Technology, Danvers, MA, USA), rabbit
450 anti-GFP (1:1000; Medical & Biological Laboratories Co., Ltd., Nagano, Japan), mouse anti-β-actin (1:1000;
451 Sigma-Aldrich). The blot was then incubated with a secondary antibody: goat anti-rabbit IgG (H+L) antibody
452 (1:5000; Thermo Fisher Scientific, Waltham, MA, USA), or Goat anti-mouse IgG (H+L) antibody (1:5000;
453 Thermo Fisher Scientific) at 27 °C for 1 h. The immunoreactive bands were visualized using Chemi-Lumi One
454 Super Kit (Nacalai Tesque) under LAS-3000 Imager (Fuji-film, Tokyo, Japan).
455
456 ***Live-cell fluorescence microscopy***
457 A confocal laser-scanning microscope (FV3000, Olympus Corporation) equipped with a stage incubator
458 (TOKAI HIT Corporation, Shizuoka, Japan) was used for live-cell imaging. All observations were performed
459 under 37 °C, 5.0 % CO_2. Cos7 cells were seeded on a 30-mm glass-bottom dish with 40 % density and
460 transfected with vectors indicated above 24 h before imaging. Time-lapse fluorescence images were captured
461 every five seconds and analyzed with ImageJ (ver 1.52a) (https://imagej.nih.gov) and GIMP software (ver
462 2.10.18).
463
464 ***Superresolution SIM live-cell imaging and analysis***

465 Superresolution structure illumination microscopy (SIM) was performed using Elyra 7 with Lattice SIM^2 (Zeiss,
466 Oberkochen, Germany). For two-color live-cell imaging, Cos7 cells with 40 % cell density were seeded on a
467 30-mm glass-bottom dish and transfected with vectors encoding EGFP-fused CLTB and mCherry-fused CIP4
468 24 h before imaging. The culture medium in the dish was exchanged with the phenol red-free DMEM (Sigma-
469 Aldrich) 30 min before imaging. Images were taken every 0.5 s and processed with Zeiss Enz 3.6 blue edition
470 software. The images were analyzed with ImageJ (ver 1.52a).
471
472 ***CD spectroscopy***
473 The circular dichroism (CD) spectra were acquired with JASCO J-805 spectropolarimeter (JASCO Corporation,
474 Tokyo, Japan) using 1.0 mL quartz cuvettes with a 5-mm path length. Purified HR1 domain was diluted with
475 1×PBS to the final concentration of 0.4 mg/mL. The measurement was performed at 25 °C in the 280 – 198 nm
476 range with a data point interval of 0.2 nm.
477
478 ***Gel-filtration chromatography***
479 The gel filtration chromatography was performed with the AKTA purifier system (GE Healthcare, Chicago, IL,
480 USA) under the control of Unicorn 5.1 software. The running buffer contains 20 mM NaCl, 25 mM HEPES,
481 and 0.2 mM 2-mercaptoethanol. Superdex 75 10/300 GL column (Cytiva) with a void volume (Vo) of 7.2 mL
482 was used. The calibration curve was obtained by plotting the molecular weight of marker proteins against the
483 partition coefficient (Kav). Kav was calculated with the equation: Kav = (Ve-Vo) / (Vt-Vo). Ve: elution volume;
484 Vo: void volume; Vt: total volume.
485
486 ***Phase separation assay***
487 Hexa-histidine-tagged recombinant proteins of CIP4-FDR, FBP17-FDR, and Synd2-IDR were used for the
488 phase separation assay. The purified protein (~10 mg/mL) was incubated with ATTO488-maleimide (Thermo
489 Fisher Scientific) at 28 °C for 1 h. The reaction was quenched by 4 mM DTT. Droplet formation was induced
490 by adding 5% polyethylene glycol and imaged by fluorescence microscopy (FV3000, Olympus Corporation).
491 For examining interaction with actin, purified actin (Cytoskeleton Inc., DENVER, CO, USA) and rhodamine-
492 labeled actin (Cytoskeleton Inc.) were reconstituted with the following buffer: 5 mM Tris-HCl (pH 8.0), 0.2

493 mM $CaCl_2$, 0.2 mM ATP, 5%(w/v) sucrose. Rhodamine-labeled and non-labeled actin were mixed at 1:20 to a
494 final concentration of 450 μg/mL and pre-incubated with Mg^{2+} (50 μM) and EGTA (0.2 mM) at 28 °C for 4
495 min. Purified CIP4-IDR was diluted to 3 mg/mL with the following buffer: 5 mM Tris-HCl (pH8.0), 1.2 mM
496 ATP, 1.1 mM DTT, 50 mM KCl, 2 mM $MgCl_2$, 5% (w/v) polyethylene glycol (Sigma-Aldrich). Mg^{2+}-charged
497 actin was then added to 45 μg/mL and observed by fluorescence microscope (FV3000).
498
499 ***Turbidity assay***
500 Recombinant proteins of hexa-histidine-tagged CIP4-FDR, FBP17-FDR, Synd2-IDR, CIP4-FDR-4S, CIP4-
501 HR1, CIP4-HR1(4S), CIP4-FDR(ΔHR1), CIP4-FDR(ΔIDR1) and CIP4-FDR(ΔIDR2) were used in the
502 turbidity assay. Purified proteins were serially diluted with Dilution Buffer (50 mM HEPES pH 7.4 and 100
503 mM NaCl), mixed with an equal volume of Droplet Buffer (30% polyethylene glycol, 50 mM HEPES, 100 mM
504 NaCl, pH 8.0), and incubated at 25 °C for 10 min. The mixture was then transferred to a micro-cuvette
505 (BRANDTech Scientific Inc., ESSEX, CT, USA), and the optical density at 600 nm was measured using a
506 spectrophotometer (JASCO V-630). The saturation concentration (C_{sat}) was obtained by fitting the data with the
507 following equation by OriginPro (v.9.8):
508 $OD_{600} = OD_{max}\ C^n / (C_{sat}^n + C^n)$,
509 where C represents protein concentration.
510
511 ***Multiple sequence alignment and three-dimensional protein structure predictions***
512 Multiple sequence alignment was performed using the T-Coffee test [69]. Sequence similarity was required using
513 EMBOSS Needle (https://www.ebi.ac.uk/Tools/psa/emboss_needle/). Three-dimensional protein structure was
514 predicted using AlphaFold2 [70].
515
516 ***Statistical analysis***
517 To analyze the closing patterns of CCPs, relatively equal numbers of CCP images were collected from four
518 different Cos7 cells. The total number of CCPs analyzed in each analysis is described in the figure legends. All

statistical analyses were performed using student's t-test, unless otherwise indicated. Differences were considered statistically significant at $P < 0.05$

References

1. Anderson, R.G., Brown, M.S., and Goldstein, J.L. (1977). Role of the coated endocytic vesicle in the uptake of receptor-bound low density lipoprotein in human fibroblasts. Cell 10, 351–364. 10.1016/0092-8674(77)90022-8.
2. Rappoport, J.Z., and Simon, S.M. (2003). Real-time analysis of clathrin-mediated endocytosis during cell migration. J. Cell Sci. 116, 847–855. 10.1242/jcs.00289.
3. Vieira, A.V., Lamaze, C., and Schmid, S.L. (1996). Control of EGF receptor signaling by clathrin-mediated endocytosis. Science 274, 2086–2089. 10.1126/science.274.5295.2086.
4. Fielding, P.E., and Fielding, C.J. (1996). Intracellular transport of low density lipoprotein derived free cholesterol begins at clathrin-coated pits and terminates at cell surface caveolae. Biochemistry 35, 14932–14938. 10.1021/bi9613382.
5. Kim, H.R., Gil, S., Andrieux, K., Nicolas, V., Appel, M., Chacun, H., Desmaele, D., Taran, F., Georgin, D., and Couvreur, P. (2007). Low-density lipoprotein receptor-mediated endocytosis of PEGylated nanoparticles in rat brain endothelial cells. Cell. Mol. Life Sci. 64, 356–364. 10.1007/s00018-007-6390-x.
6. Brodin, L., Löw, P., and Shupliakov, O. (2000). Sequential steps in clathrin-mediated synaptic vesicle endocytosis. Curr. Opin. Neurobiol. 10, 312–320. 10.1016/s0959-4388(00)00097-0.
7. Kaksonen, M., Toret, C.P., and Drubin, D.G. (2005). A modular design for the clathrin-and actin-mediated endocytosis machinery. Cell 123, 305–320. 10.1016/j.cell.2005.09.024.
8. Weinberg, J., and Drubin, D.G. (2012). Clathrin-mediated endocytosis in budding yeast. Trends Cell Biol. 22, 1–13. 10.1016/j.tcb.2011.09.001.
9. Taylor, M.J., Perrais, D., and Merrifield, C.J. (2011). A high precision survey of the molecular dynamics of mammalian clathrin-mediated endocytosis. PLoS Biol. 9, e1000604. 10.1371/journal.pbio.1000604.

546 10. Hussain, N.K., Jenna, S., Glogauer, M., Quinn, C.C., Wasiak, S., Guipponi, M., Antonarakis, S.E.,
547 Kay, B.K., Stossel, T.P., and Lamarche-Vane, N. (2001). Endocytic protein intersectin-l regulates
548 actin assembly via Cdc42 and N-WASP. Nat. Cell Biol. 3, 927–932. 10.1038/ncb1001-927.
549 11. Yamabhai, M., Hoffman, N.G., Hardison, N.L., McPherson, P.S., Castagnoli, L., Cesareni, G., and
550 Kay, B.K. (1998). Intersectin, a novel adaptor protein with two Eps15 homology and five Src
551 homology 3 domains. J. Biol. Chem. 273, 31401–31407. 10.1074/jbc.273.47.31401.
552 12. Collins, B.M., McCoy, A.J., Kent, H.M., Evans, P.R., and Owen, D.J. (2002). Molecular architecture
553 and functional model of the endocytic AP2 complex. Cell 109, 523–535. 10.1016/s0092-
554 8674(02)00735-3.
555 13. Kadlecova, Z., Spielman, S.J., Loerke, D., Mohanakrishnan, A., Reed, D.K., and Schmid, S.L. (2017).
556 Regulation of clathrin-mediated endocytosis by hierarchical allosteric activation of AP2. J. Cell Biol.
557 216, 167–179. 10.1083/jcb.201608071.
558 14. Henne, W.M., Boucrot, E., Meinecke, M., Evergren, E., Vallis, Y., Mittal, R., and McMahon, H.T.
559 (2010). FCHo proteins are nucleators of clathrin-mediated endocytosis. Science 328, 1281–1284.
560 10.1126/science.1188462.
561 15. Kirchhausen, T., and Harrison, S.C. (1981). Protein organization in clathrin trimers. Cell 23, 755–761.
562 10.1016/0092-8674(81)90439-6.
563 16. Nossal, R. (2001). Energetics of clathrin basket assembly. Traffic 2, 138–147. 10.1034/j.1600-
564 0854.2001.020208.x.
565 17. Hinshaw, J.E., and Schmid, S.L. (1995). Dynamin self-assembles into rings suggesting a mechanism
566 for coated vesicle budding. Nature 374, 190–192. 10.1038/374190a0.
567 18. Shnyrova, A.V., Bashkirov, P.V., Akimov, S.A., Pucadyil, T.J., Zimmerberg, J., Schmid, S.L., and
568 Frolov, V.A. (2013). Geometric catalysis of membrane fission driven by flexible dynamin rings.
569 Science 339, 1433–1436. 10.1126/science.1233920.
570 19. Galletta, B.J., Mooren, O.L., and Cooper, J.A. (2010). Actin dynamics and endocytosis in yeast and
571 mammals. Curr. Opin. Biotechnol. 21, 604–610. 10.1016/j.copbio.2010.06.006.
572 20. Mund, M., van der Beek, J.A., Deschamps, J., Dmitrieff, S., Hoess, P., Monster, J.L., Picco, A.,
573 Nédélec, F., Kaksonen, M., and Ries, J. (2018). Systematic nanoscale analysis of endocytosis links

574 efficient vesicle formation to patterned actin nucleation. Cell 174, 884–896. e817.
575 10.1016/j.cell.2018.06.032.
576 21. Boulant, S., Kural, C., Zeeh, J.-C., Ubelmann, F., and Kirchhausen, T. (2011). Actin dynamics
577 counteract membrane tension during clathrin-mediated endocytosis. Nat. Cell Biol. 13, 1124–1131.
578 10.1038/ncb2307.
579 22. Collins, A., Warrington, A., Taylor, K.A., and Svitkina, T. (2011). Structural organization of the actin
580 cytoskeleton at sites of clathrin-mediated endocytosis. Curr. Biol. 21, 1167–1175.
581 10.1016/j.cub.2011.05.048.
582 23. Yang, C., Colosi, P., Hugelier, S., Zabezhinsky, D., Lakadamyali, M., and Svitkina, T. (2022). Actin
583 polymerization promotes invagination of flat clathrin-coated lattices in mammalian cells by pushing at
584 lattice edges. Nat. Commun. 13, 6127. 10.1038/s41467-022-33852-2.
585 24. Tsujita, K., Suetsugu, S., Sasaki, N., Furutani, M., Oikawa, T., and Takenawa, T. (2006).
586 Coordination between the actin cytoskeleton and membrane deformation by a novel membrane
587 tubulation domain of PCH proteins is involved in endocytosis. J. Cell Biol. 172, 269–279.
588 10.1083/jcb.200508091.
589 25. Grassart, A., Cheng, A.T., Hong, S.H., Zhang, F., Zenzer, N., Feng, Y., Briner, D.M., Davis, G.D.,
590 Malkov, D., and Drubin, D.G. (2014). Actin and dynamin2 dynamics and interplay during clathrin-
591 mediated endocytosis. J. Cell Biol. 205, 721–735. 10.1083/jcb.201403041.
592 26. Ferguson, S., Raimondi, A., Paradise, S., Shen, H., Mesaki, K., Ferguson, A., Destaing, O., Ko, G.,
593 Takasaki, J., and Cremona, O. (2009). Coordinated actions of actin and BAR proteins upstream of
594 dynamin at endocytic clathrin-coated pits. Dev. Cell 17, 811–822. 10.1016/j.devcel.2009.11.005.
595 27. Jin, M., Shirazinejad, C., Wang, B., Yan, A., Schöneberg, J., Upadhyayula, S., Xu, K., and Drubin,
596 D.G. (2022). Branched actin networks are organized for asymmetric force production during clathrin-
597 mediated endocytosis in mammalian cells. Nat. Commun. 13, 3578. 10.1038/s41467-022-31207-5.
598 28. Yarar, D., Waterman-Storer, C.M., and Schmid, S.L. (2005). A dynamic actin cytoskeleton functions
599 at multiple stages of clathrin-mediated endocytosis. Mol. Biol. Cell 16, 964–975. 10.1091/mbc.e04-
600 09-0774.

601 29. Shevchuk, A.I., Novak, P., Taylor, M., Diakonov, I.A., Ziyadeh-Isleem, A., Bitoun, M., Guicheney,
602 P., Lab, M.J., Gorelik, J., and Merrifield, C.J. (2012). An alternative mechanism of clathrin-coated pit
603 closure revealed by ion conductance microscopy. J. Cell Biol. 197, 499–508. 10.1083/jcb.201109130.
604 30. Yoshida, A., Sakai, N., Uekusa, Y., Imaoka, Y., Itagaki, Y., Suzuki, Y., and Yoshimura, S.H. (2018).
605 Morphological changes of plasma membrane and protein assembly during clathrin-mediated
606 endocytosis. PLoS Biol. 16, e2004786. 10.1371/journal.pbio.2004786.
607 31. Vasan, R., Rudraraju, S., Akamatsu, M., Garikipati, K., and Rangamani, P. (2020). A mechanical
608 model reveals that non-axisymmetric buckling lowers the energy barrier associated with membrane
609 neck constriction. Soft Matter 16, 784–797. 10.1039/c9sm01494b.
610 32. Hetrick, B., Han, M.S., Helgeson, L.A., and Nolen, B.J. (2013). Small molecules CK-666 and CK-869
611 inhibit actin-related protein 2/3 complex by blocking an activating conformational change. Chem.
612 Biol. 20, 701–712. 10.1016/j.chembiol.2013.03.019.
613 33. Ilatovskaya, D.V., Chubinskiy-Nadezhdin, V., Pavlov, T.S., Shuyskiy, L.S., Tomilin, V., Palygin, O.,
614 Staruschenko, A., and Negulyaev, Y.A. (2013). Arp2/3 complex inhibitors adversely affect actin
615 cytoskeleton remodeling in the cultured murine kidney collecting duct M-1 cells. Cell Tissue Res.
616 354, 783–792. 10.1007/s00441-013-1710-y.
617 34. Rohatgi, R., Ma, L., Miki, H., Lopez, M., Kirchhausen, T., Takenawa, T., and Kirschner, M.W.
618 (1999). The interaction between N-WASP and the Arp2/3 complex links Cdc42-dependent signals to
619 actin assembly. Cell 97, 221–231. 10.1016/s0092-8674(00)80732-1.
620 35. Qualmann, B., Koch, D., and Kessels, M.M. (2011). Let's go bananas: revisiting the endocytic BAR
621 code. EMBO J. 30, 3501–3515. 10.1038/emboj.2011.266.
622 36. Armstrong, G., and Olson, M.F. (2022). Bending Over Backwards: BAR Proteins and The Actin
623 Cytoskeleton in Mammalian Receptor-Mediated Endocytosis. Eur. J. Cell Biol., 151257.
624 10.1016/j.ejcb.2022.151257.
625 37. Aspenström, P. (2008). Roles of F-BAR/PCH proteins in the regulation of membrane dynamics and
626 actin reorganization. Int. Rev. Cell Mol. Biol. 272, 1–31. 10.1016/S1937-6448(08)01601-8.
627 38. Fricke, R., Gohl, C., Dharmalingam, E., Grevelhörster, A., Zahedi, B., Harden, N., Kessels, M.,
628 Qualmann, B., and Bogdan, S. (2009). Drosophila Cip4/Toca-1 integrates membrane trafficking and

629 actin dynamics through WASP and SCAR/WAVE. Curr. Biol. 19, 1429–1437.
630 10.1016/j.cub.2009.07.058.
631 39. Prehoda, K.E., Scott, J.A., Mullins, R.D., and Lim, W.A. (2000). Integration of multiple signals
632 through cooperative regulation of the N-WASP-Arp2/3 complex. Science 290, 801–806.
633 10.1126/science.290.5492.801.
634 40. Ho, H.-Y.H., Rohatgi, R., Lebensohn, A.M., Ma, L., Li, J., Gygi, S.P., and Kirschner, M.W. (2004).
635 Toca-1 mediates Cdc42-dependent actin nucleation by activating the N-WASP-WIP complex. Cell
636 118, 203–216. 10.1016/j.cell.2004.06.027.
637 41. Tian, L., Nelson, D.L., and Stewart, D.M. (2000). Cdc42-interacting protein 4 mediates binding of the
638 Wiskott-Aldrich syndrome protein to microtubules. J. Biol. Chem. 275, 7854–7861.
639 10.1074/jbc.275.11.7854.
640 42. Aspenström, P. (1997). A Cdc42 target protein with homology to the non-kinase domain of FER has a
641 potential role in regulating the actin cytoskeleton. Curr. Biol. 7, 479–487. 10.1016/s0960-
642 9822(06)00219-3.
643 43. Yamazaki, H., Takagi, M., Kosako, H., Hirano, T., and Yoshimura, S.H. (2022). Cell cycle-specific
644 phase separation regulated by protein charge blockiness. Nat. Cell Biol. 24, 625–632.
645 10.1038/s41556-022-00903-1.
646 44. Lin, Y.-H., Forman-Kay, J.D., and Chan, H.S. (2016). Sequence-specific polyampholyte phase
647 separation in membraneless organelles. Phys. Rev. Lett. 117, 178101.
648 10.1103/PhysRevLett.117.178101.
649 45. Danielsen, S.P., McCarty, J., Shea, J.-E., Delaney, K.T., and Fredrickson, G.H. (2019). Molecular
650 design of self-coacervation phenomena in block polyampholytes. Proc. Natl. Acad. Sci. U. S. A. 116,
651 8224–8232. 10.1073/pnas.1900435116.
652 46. Zeno, W.F., Baul, U., Snead, W.T., DeGroot, A., Wang, L., Lafer, E.M., Thirumalai, D., and
653 Stachowiak, J.C. (2018). Synergy between intrinsically disordered domains and structured proteins
654 amplifies membrane curvature sensing. Nat. Commun. 9, 4152. 10.1038/s41467-018-06532-3.

655 47. Su, M., Zhuang, Y., Miao, X., Zeng, Y., Gao, W., Zhao, W., and Wu, M. (2020). Comparative Study
656 of Curvature Sensing Mediated by F-BAR and an Intrinsically Disordered Region of FBP17. iScience
657 23, 101712. 10.1016/j.isci.2020.101712.
658 48. Zeno, W.F., Snead, W.T., Thatte, A.S., and Stachowiak, J.C. (2019). Structured and intrinsically
659 disordered domains within Amphiphysin1 work together to sense and drive membrane curvature. Soft
660 Matter 15, 8706–8717. 10.1039/c9sm01495k.
661 49. Zeno, W.F., Thatte, A.S., Wang, L., Snead, W.T., Lafer, E.M., and Stachowiak, J.C. (2019).
662 Molecular mechanisms of membrane curvature sensing by a disordered protein. J. Am. Chem. Soc.
663 141, 10361–10371. 10.1021/jacs.9b03927.
664 50. Busch, D.J., Houser, J.R., Hayden, C.C., Sherman, M.B., Lafer, E.M., and Stachowiak, J.C. (2015).
665 Intrinsically disordered proteins drive membrane curvature. Nat. Commun. 6, 7875.
666 10.1038/ncomms8875.
667 51. Snead, W.T., Zeno, W.F., Kago, G., Perkins, R.W., Richter, J.B., Zhao, C., Lafer, E.M., and
668 Stachowiak, J.C. (2019). BAR scaffolds drive membrane fission by crowding disordered domains. J.
669 Cell Biol. 218, 664–682. 10.1083/jcb.201807119.
670 52. Stachowiak, J.C., Schmid, E.M., Ryan, C.J., Ann, H.S., Sasaki, D.Y., Sherman, M.B., Geissler, P.L.,
671 Fletcher, D.A., and Hayden, C.C. (2012). Membrane bending by protein–protein crowding. Nat. Cell
672 Biol. 14, 944–949. 10.1038/ncb2561.
673 53. Yuan, F., Alimohamadi, H., Bakka, B., Trementozzi, A.N., Day, K.J., Fawzi, N.L., Rangamani, P.,
674 and Stachowiak, J.C. (2021). Membrane bending by protein phase separation. Proc. Natl. Acad. Sci.
675 U. S. A. 118, e2017435118. 10.1073/pnas.2017435118.
676 54. Dawson, J.C., Legg, J.A., and Machesky, L.M. (2006). Bar domain proteins: a role in tubulation,
677 scission and actin assembly in clathrin-mediated endocytosis. Trends Cell Biol. 16, 493–498.
678 10.1016/j.tcb.2006.08.004.
679 55. Heath, R.J., and Insall, R.H. (2008). F-BAR domains: multifunctional regulators of membrane
680 curvature. J. Cell Sci. 121, 1951–1954. 10.1242/jcs.023895.
681 56. Watson, J.R., Fox, H.M., Nietlispach, D., Gallop, J.L., Owen, D., and Mott, H.R. (2016).
682 Investigation of the interaction between Cdc42 and its effector TOCA1: handover of Cdc42 to the

683 actin regulator N-WASP is facilitated by differential binding affinities. J. Biol. Chem. 291, 13875–
684 13890. 10.1074/jbc.M116.724294.
685 57. Taylor, K.L., Taylor, R.J., Richters, K.E., Huynh, B., Carrington, J., McDermott, M.E., Wilson, R.L.,
686 and Dent, E.W. (2019). Opposing functions of F-BAR proteins in neuronal membrane protrusion,
687 tubule formation, and neurite outgrowth. Life Sci. Alliance 2, e201800288. 10.26508/lsa.201800288.
688 58. Ledoux, B., Zanin, N., Yang, J., Coster, C., Dupont-Gillain, C., Alsteens, D., Morsomme, P., and
689 Renard, H.-F. (2022). Plasma membrane nanodeformations promote actin polymerisation through
690 CIP4/CDC42 recruitment and regulate type II IFN signaling. bioRxiv. 10.1101/2022.08.16.504113.
691 59. Hak, L.C.W., Khan, S., Di Meglio, I., Law, A.-L., Häsler, S.L.-A., Quintaneiro, L.M., Ferreira, A.P.,
692 Krause, M., McMahon, H.T., and Boucrot, E. (2018). FBP17 and CIP4 recruit SHIP2 and
693 lamellipodin to prime the plasma membrane for fast endophilin-mediated endocytosis. Nat. Cell Biol.
694 20, 1023–1031. 10.1038/s41556-018-0146-8.
695 60. Leibfried, A., Fricke, R., Morgan, M.J., Bogdan, S., and Bellaiche, Y. (2008). Drosophila Cip4 and
696 WASp define a branch of the Cdc42-Par6-aPKC pathway regulating E-cadherin endocytosis. Curr.
697 Biol. 18, 1639–1648. 10.1016/j.cub.2008.09.063.
698 61. Shimada, A., Niwa, H., Tsujita, K., Suetsugu, S., Nitta, K., Hanawa-Suetsugu, K., Akasaka, R.,
699 Nishino, Y., Toyama, M., and Chen, L. (2007). Curved EFC/F-BAR-domain dimers are joined end to
700 end into a filament for membrane invagination in endocytosis. Cell 129, 761–772.
701 10.1016/j.cell.2007.03.040.
702 62. Kobashigawa, Y., Kumeta, H., Kanoh, D., and Inagaki, F. (2009). The NMR structure of the TC10-
703 and Cdc42-interacting domain of CIP4. J. Biomol. NMR 44, 113–118. 10.1007/s10858-009-9317-z.
704 63. Graham, K.D., Chandrasekaran, A., Wang, L., Ladak, A., Lafer, E.M., Rangamani, P., and
705 Stachowiak, J.C. (2022). Liquid-like assembly of VASP drives actin polymerization and bundling.
706 bioRxiv. 10.1101/2022.05.09.491236.
707 64. Yang, S., Liu, C., Guo, Y., Li, G., Li, D., Yan, X., and Zhu, X. (2022). Self-construction of actin
708 networks through phase separation–induced abLIM1 condensates. Proc. Natl. Acad. Sci. U. S. A. 119,
709 e2122420119. 10.1073/pnas.2122420119.

710 65. Nalbant, P., Hodgson, L., Kraynov, V., Toutchkine, A., and Hahn, K.M. (2004). Activation of
711 endogenous Cdc42 visualized in living cells. Science 305, 1615–1619. 10.1126/science.1100367.
712 66. Ma, L., Cantley, L.C., Janmey, P.A., and Kirschner, M.W. (1998). Corequirement of specific
713 phosphoinositides and small GTP-binding protein Cdc42 in inducing actin assembly in Xenopus egg
714 extracts. J. Cell. Biol. 140, 1125–1136. 10.1083/jcb.140.5.1125.
715 67. Zhang, Y., Yoshida, A., Sakai, N., Uekusa, Y., Kumeta, M., and Yoshimura, S.H. (2017). In vivo
716 dynamics of the cortical actin network revealed by fast-scanning atomic force microscopy.
717 Microscopy 66, 272–282. 10.1093/jmicro/dfx015.
718 68. Yoshida, A., Sakai, N., Uekusa, Y., Deguchi, K., Gilmore, J.L., Kumeta, M., Ito, S., and Takeyasu, K.
719 (2015). Probing in vivo dynamics of mitochondria and cortical actin networks using high-speed
720 atomic force/fluorescence microscopy. Genes Cells 20, 85–94. 10.1111/gtc.12204.
721 69. Notredame, C., Higgins, D.G., and Heringa, J. (2000). T-Coffee: A novel method for fast and accurate
722 multiple sequence alignment. J. Mol. Biol. 302, 205–217. 10.1006/jmbi.2000.4042.
723 70. Jumper, J., Evans, R., Pritzel, A., Green, T., Figurnov, M., Ronneberger, O., Tunyasuvunakool, K.,
724 Bates, R., Žídek, A., and Potapenko, A. (2021). Highly accurate protein structure prediction with
725 AlphaFold. Nature 596, 583–589. 10.1038/s41586-021-03819-2.
726

Supplemental Information

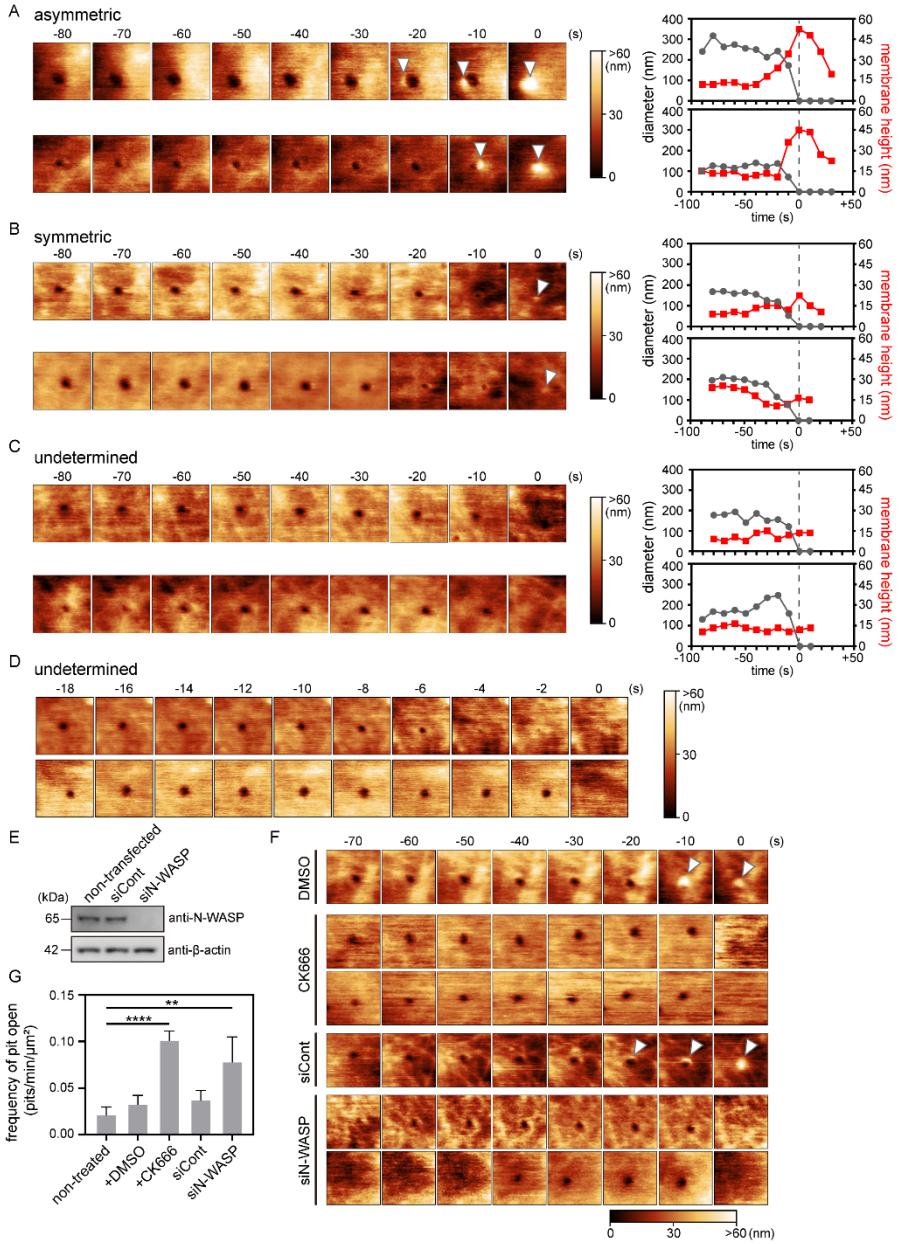

Figure S1. Asymmetric closing pattern of the CCP, related to Figure 1.

A–C. Additional examples of the time-lapse HS-AFM images of asymmetric (A), symmetric (B), and undetermined (C) closing patterns obtained from Cos7 cells. Details of the experimental conditions and data presentations are the same as those in Figure 1A and C.

D. Time-lapse HA-AFM images of CCPs with the undetermined closing pattern at a scanning rate of 2 s/frame. Time 0 was defined as the time point when the pit completely closed on the HS-AFM image. The height information of the AFM image is presented using a color bar. Image size: $1.0 \times 1.0\ \mu m^2$.

E. Knockdown efficiency of N-WASP. The total cell lysate of non-transfected Cos7 cells and Cos7 cells transfected with siRNA for the control (luciferase) or N-WASP was prepared 48 h after the transfection and then subjected to the western blot analysis using anti-N-WASP antibody. β-actin was detected as an internal control.

F. Time-lapse HS-AFM images obtained from Cos7 cells treated with DMSO or CK666 and cells transfected with siRNA for the control (luciferase) or N-WASP. Images were taken every 10 s. Time 0 was defined as the time point when the pit completely closed on the HS-AFM image. The membrane bulge is indicated by arrowheads and the height information of the AFM image is presented using a color bar. Image size: $1.0 \times 1.0\ \mu m^2$.

G. The frequency of CCP formation in non-treated Cos7 cells, the cells treated with DMSO or CK666, and the cells transfected with siRNA for the control (luciferase) or N-WASP was quantified and summarized. Statistical analysis was performed using Student's t-test, $\alpha = 0.05$; **:$P < 0.01$; ****: $P < 0.0001$. Data are presented as mean ± standard deviation from four independent experiments.

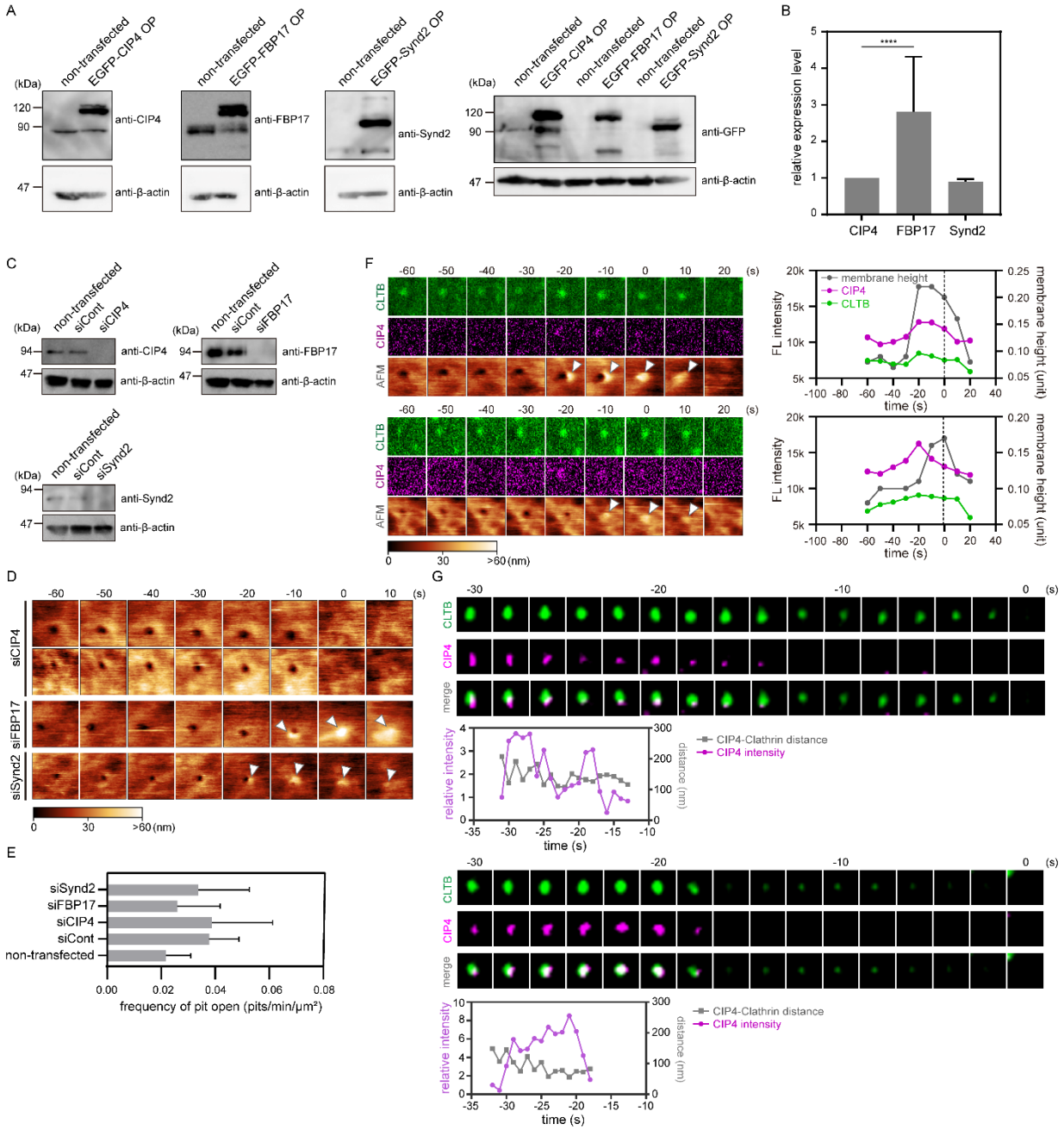
A
non-transfected
EGFP-CIP4 OP
EGFP-FBP17 OP
EGFP-Synd2 OP
(kDa)
120
90
47
anti-CIP4
anti-FBP17
anti-Synd2
anti-GFP
anti-β-actin
B
relative expression level
****
CIP4
FBP17
Synd2
C
siCont
siCIP4
siFBP17
siSynd2
94
D
siCIP4
siFBP17
siSynd2
(s)
0
30
>60 (nm)
E
siSynd2
siFBP17
siCIP4
siCont
non-transfected
0.00
0.02
0.04
0.06
0.08
frequency of pit open (pits/min/μm²)
F
CLTB
CIP4
AFM
membrane height
FL intensity
membrane height (unit)
time (s)
G
merge
CIP4-Clathrin distance
CIP4 intensity
relative intensity
distance (nm)

731

Figure S2. CIP4 is necessary for the asymmetric bulge, related to Figure 2.

A. The endogenous amount of CIP4, FBP17, and Synd2 in Cos7 cells was examined using western blotting. The total cell lysate of Cos7 cells expressing EGFP-fused CIP4, FBP17, or Synd2 was subjected to western blotting using anti-CIP4, -FBP17, or -Synd2 antibody, respectively. The same lysate was also blotted with an anti-GFP antibody for reference. The amount of β-actin was detected with an anti-β-actin antibody as an internal control.

B. The endogenous amount of CIP4, FBP17, and Synd2 obtained from western blotting is shown in (A). Data from the three independent experiments are summarized. Statistical analysis was performed using Student's t-test, $\alpha = 0.05$; ****: $P < 0.0001$. Data are presented as mean ± standard deviation from three independent experiments as a relative value to that of CIP4.

C. Knockdown efficiency of CIP4, FBP17, and Synd2 in Cos7 cells. Total cell lysate of non-transfected Cos7 cells and Cos7 cells transfected with siRNA for the control (luciferase), CIP4, FBP17, or Synd2 was prepared 48 h after the transfection and then subjected to the western blot analysis using anti-CIP4, FBP17, or Synd2 antibodies. β-actin was detected as an internal control.

D. Additional examples of the time-lapse HS-AFM images obtained from Cos7 cells transfected with siRNA against CIP4, Synd2, or FBP17. Details of the experimental conditions and data presentations are the same as those in Figure 2C.

E. The frequency of CCP formation in non-transfected Cos7 cells and Cos7 cells transfected with siRNA for the control (luciferase), CIP4, FBP17, or Synd2 was quantified and summarized. Statistical analysis was performed using Student's t-test, $\alpha = 0.05$. There was no significant differences between any two groups. Data are presented as mean ± standard deviation from four independent experiments.

F. Additional examples of the correlative imaging of HS-AFM and confocal laser scanning microscopy (CLSM). The fluorescent (FL) intensity of EGFP-fused CLTB and mCherry-fused CIP4 and the maximum membrane height at the CCP area were plotted against time. Time 0 was defined as the time when the pit completely closed and is indicated with a black dotted line. Other details of the experimental conditions and data presentations are the same as those in Figure 2D.

G. Additional examples of the time-lapse superresolution SIM images obtained from Cos7 cells expressing EGFP-fused CLTB and mCherry-fused CIP4. Details of the experimental conditions and data presentations are the same as those in Figure 2E.

732

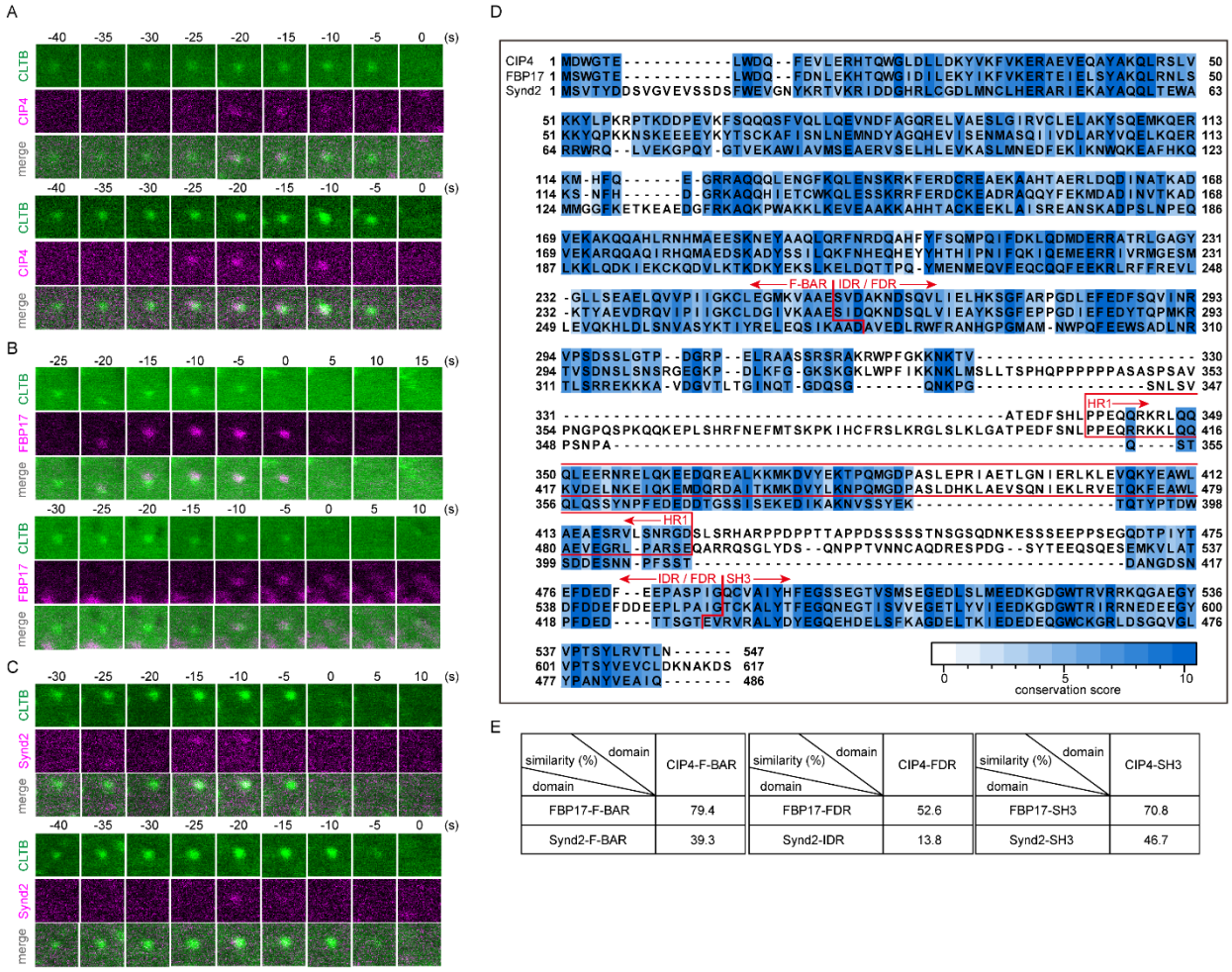

Figure S3. Assembly of F-BAR proteins CIP4, FBP17, and Synd2 to CCP, related to Figure 2 and Figure 3.

A–C. Additional examples of the time-lapse fluorescence images obtained from Cos7 cells expressing EGFP-fused CLTB and mCherry-fused CIP4 (A), FBP17 (B), or Synd2 (C). Details of the experimental conditions and data presentations are same as those in Figure 2A

D. Amino-acid sequence alignment of *Mus musculus* CIP4 (Uniprot, Q8CJ53-3), *Homo sapiens* FBP17 (Uniprot, Q96RU3), and *Mus musculus* Synd2 (Uniprot, Q9WVE8). Alignment was performed by Tcoffee (see Method). The conservation was scored and presented as shown in a color bar. The F-BAR, FDR/IDR, HR1, and SH3 domains are indicated.

E. Pairwise-domain similarity among CIP4, FBP17, and Synd2. The analysis was performed by EMBOSS Needle.

733

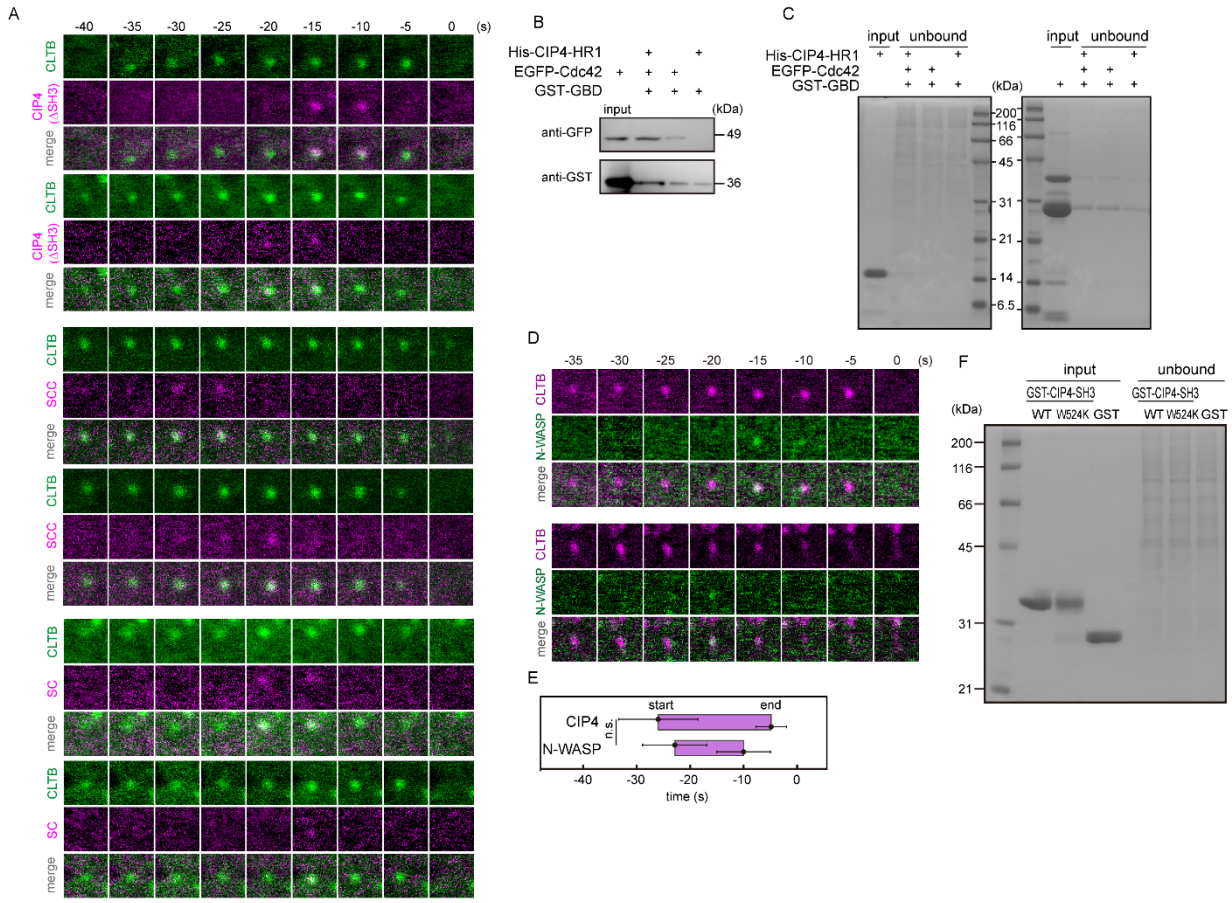

Figure S4. FDR and SH3 domain are necessary for the asymmetric bulge, related to Figure 3.

A. Additional examples of the time-lapse fluorescence images obtained from Cos7 cells expressing EGFP-fused CLTB and mCherry-fused chimeric CIP4 molecules. Details of the experimental conditions and data presentations are the same as those in Figure 3B.

B, C. Pull-down assay among CIP4-HR1, Cdc42, and the GBD of N-WASP. GST-tagged GBD was incubated with or without hexahistidine-tagged CIP4-HR1 domain and the cell lysate containing EGFP-fused Cdc42. The eluted fractions were subjected to the western blot analysis using anti-GFP antibody (B). The input amount of CIP4-HR1 and the unbound fraction were analyzed using SDS-PAGE (C).

D. Time-lapse fluorescence images of EGFP-fused N-WASP and mCherry-fused CLTB expressed in Cos7 cells. Time 0 was defined as the time when the clathrin signal disappeared. Image size: 1.0 ×1.0 μm^2.

E. A summary of the assembly profile of CIP4 and N-WASP at CCPs. Time 0 was defined as the time when the clathrin signal disappeared. The timing when the fluorescence signal appeared and disappeared at the CCP area was defined as "start" and "end," respectively, and are plotted as mean ± standard deviation (N = 20, for each condition). Statistical analysis was performed using the Student's t-test, $\alpha = 0.05$; n.s., not significant ($P > 0.05$).

F. Input amount of GST-tagged CIP4-SH3(WT), CIP4-SH3(W524K), and empty GST and the unbound fraction of the pulldown assay in Figure 3E was analyzed using SDS-PAGE.

734

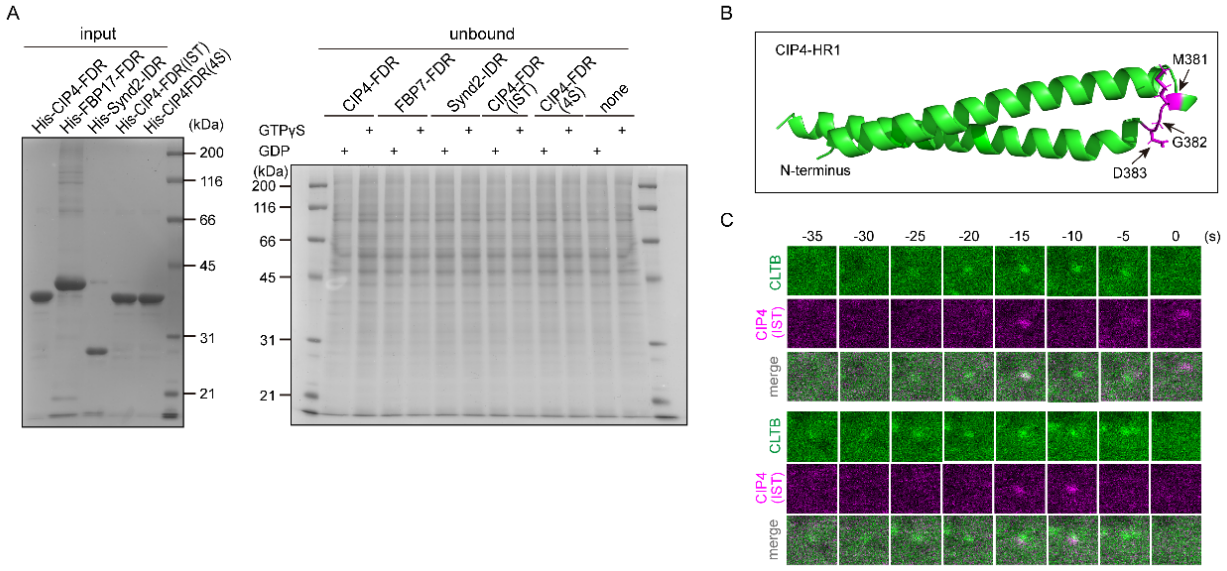

Figure S5. Cdc42 recruits CIP4 to the site of CCP, related to Figure 4.

A. SDS-PAGE analysis of the input and the unbound fraction of the pulldown assay shown in Figure 4A.

B. A three-dimensional structure of CIP4-HR1 predicted by AlphaFold2. Three mutated residues in the CIP4(IST) (M381, G382, D383) are shown in magenta.

C. Additional examples of the time-lapse fluorescence images of EGFP-fused CLTB and mCherry-fused CIP4(IST) expressed in Cos7 cells. Details of the experimental conditions and data presentations are the same as those in Figure 4B.

735

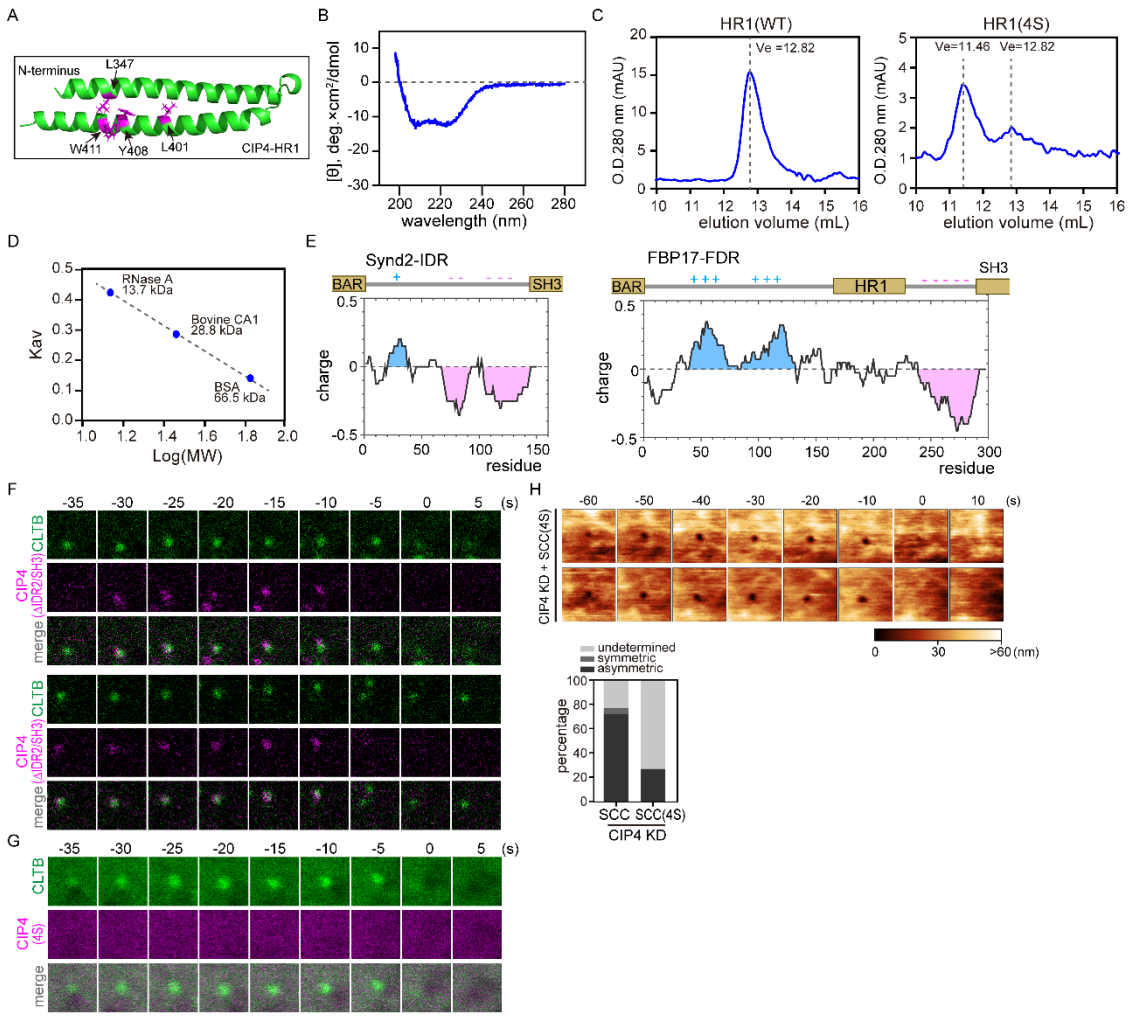

736

Figure S6. Structural and functional properties of FDRs, related to Figure 5.

A. Three-dimensional structure of the CIP4-HR1 domain predicted using AlphaFold2. The mutated residues in the CIP4-HR1(4S) are shown in magenta.

B. A circular dichroism spectrum of purified CIP4-HR1.

C. Gel filtration chromatography of CIP4-HR1(WT), and CIP4-HR1(4S). The absorbance at 280 nm (mAU) is plotted against the elution volume (mL). The peak position (Ve) was indicated with a dotted line.

D. A size calibration of gel filtration chromatography shown in B. RNase A (13.7 kDa), bovin carbonic anhydrase 1 (bovin CA-1, 28.8 kDa), and bovine serum albumin (BSA, 66.5 kDa) were analyzed. The partition coefficient (K_{av}) obtained from the chromatogram is plotted against the molecular weight.

E. Charge plot of Synd2-IDR and FBP17-FDR. Positively and negatively charged regions are marked in blue and red, respectively.

F. Additional examples of the time-lapse fluorescence images of EGFP-fused CLTB and mCherry-fused CIP4 (□IDR2/SH3) expressed in Cos7 cells. Details of the experimental conditions and data presentations are the same as those in Figure 5E.

G. Time-lapse fluorescence images of EGFP-fused CLTB and mCherry-fused CIP4(4S) expressed in Cos7 cells. Image size: 1.0 ×1.0 μm^2. The time point of the disappearance of the clathrin signal was defined as "0 s."

H. Time-lapse HS-AFM images obtained from Cos7 cells expressing EGFP-fused SCC(4S) under the CIP4-KD background. Images were taken every 10 s. Time 0 was defined as the time point when the pit completely closed on the HS-AFM image. The height information of the AFM image is presented using a color bar. Image size: 1.0 × 1.0 μm^2. The frequency of three different closing patterns was measured and summarized in the bottom panel (N = 60, for each condition).

737

Video S1. Morphological changes of the plasma membrane during the asymmetric CCP closing, related to Figure 1.

Representative movie of the asymmetric CCP closing in Cos7 cells captured by HS-AFM. Images were taken every 2 s. The height information of the AFM image is presented using a color bar. Image size on the x-y plane: $1.0 \times 1.0\ \mu m^2$.